BRNO UNIVERSITY OF TECHNOLOGY

Faculty of Electrical Engineering
and Communication

MASTER'S THESIS

Brno, 2018 Bc. Kateřina Nováková

BRNO UNIVERSITY OF TECHNOLOGY

VYSOKÉ UČENÍ TECHNICKÉ V BRNĚ

FACULTY OF ELECTRICAL ENGINEERING AND COMMUNICATION

FAKULTA ELEKTROTECHNIKY
A KOMUNIKAČNÍCH TECHNOLOGIÍ

DEPARTMENT OF BIOMEDICAL ENGINEERING

ÚSTAV BIOMEDICÍNSKÉHO INŽENÝRSTVÍ

USING BLIND IMAGE FILTERING FOR IMAGES FROM TEM MICROSCOPES

VYUŽITIE SLEPEJ FILTRÁCIE OBRAZU PRE SNÍMKY Z TEM MIKROSKOPOV

MASTER'S THESIS
DIPLOMOVÁ PRÁCE

AUTHOR — **Bc. Kateřina Nováková**
AUTOR PRÁCE

SUPERVISOR — **Ing. Tomáš Potočňák**
VEDOUCÍ PRÁCE

BRNO 2018

BRNO UNIVERSITY OF TECHNOLOGY
FACULTY OF ELECTRICAL ENGINEERING AND COMMUNICATION

Master's Thesis

Master's study field **Biomedical and Ecological Engineering**
Department of Biomedical Engineering

Student: Bc. Kateřina Nováková ***ID:*** 165015

Year of study: 2 ***Academic year:*** 2017/18

TITLE OF THESIS:

Using blind image filtering for images from TEM microscopes

INSTRUCTION:

1) Elaborate a literary research in the area of blind image filtering (filtering without the knowledge of noise character). Study the applicability of these methods on images from the Transverse Electron Microscope (TEM). 2) Choose theoretically the most appropriate approach to blind filtering for images from TEM microscopes. 3) Define a way of evaluating the results according to the acquisition parameters of the electron microscope. 4) Create a test set of images in collaboration with FEI Czech Republic (part of Thermo Fisher Scientific). 5) Test the selected methods on model and real images and compare the results with the commercially available methods. Process the selected algorithms in Matlab or Python. 6) Discuss the results obtained and evaluate the efficiency and usability of the methods. The diploma thesis is created in cooperation with the FEI of the Czech Republic (part of Thermo Fisher Scientific).

RECOMMENDED LITERATURE:

[1] KARLIK M., Úvod do transmisní elektronové mirkoskopie. Praha ČVUT, 2011. ISBN 978-80-01-04729-3.

[2] JAN, J. Digital Signal Filtering, Analysis and Restoration. volume 44. volume 44. London: The Institution of Electrical Engineers, 2000. 407 s. ISBN: 0-85296-760- 8.

Date of project specification: 5.2.2018 ***Deadline for submission:*** 18.5.2018

Leader: Ing. Tomáš Potočňák
Consultant:

prof. Ing. Ivo Provazník, Ph.D.
Subject Council chairman

ABSTRAKT

Předložená práce se zabývá problematikou slepé filtrace obrazů z transmisního elektronového mikroskopu. V úvodu práce je uveden popis transmisního elektronového mikroskopu. Navazující část popisuje mechanismy interakce elektronů se zkoumaným vzorkem a z toho vyplývající zobrazovací techniky elektronové mikroskopie. Poslední kapitola teoretické části práce zahrnuje popis vybraných metod slepé filtrace obrazu zejména s využitím dekompozice obrazu na charakteristické složky. Taktéž je zde uveden výčet metod pro zhodnocení úspěšnosti filtrace. V praktické části jsou popsány aplikované metody slepé filtrace obrazů a výsledky filtrování. Jednotlivé metody jsou mezi sebou porovnány. Získané výsledky a využitelnost aplikovaných metod jsou zhodnoceny v diskuzi.

KLÍČOVÁ SLOVA

TEM, transmisní elektronová mikroskopie, slepá filtrace, EMD, SVD, ICA.

ABSTRACT

This work deals with the blind filtration of the images from the transmission electron microscope. At the beginning of this work there is a basic description of the transmission electron microscope. Following part describes the mechanisms of electron interactions with the observed specimen. Description of basic electron microscopy imaging techniques is included. The last chapter of the theoretical part includes the description of several chosen blind image filtration techniques, especially those using the decomposition of the image into characteristic components. It also contains a summary of methods for evaluation the filtration effectiveness. The practical part focuses on a description of applied blind filtering methods and brings the results of the filtration. Individual methods are compared. In conclusion, the obtained results and usability of the applied methods are discussed.

KEYWORDS

TEM, transmission electron microscopy, blind filtering, EMD, SVD, ICA.

NOVÁKOVÁ, K. *Using blind image filtering for images from TEM microscopes*. Brno: Brno University of Technology, Faculty of Electrical Engineering and Communication, 2018. 87 p. Advised by Ing. Tomáš Potočňák.

PROHLÁŠENÍ

Prohlašuji, že svou diplomovou práci na téma Využitie slepej filtrácie obrazu pre snímky z TEM mikroskopov jsem vypracovala samostatně pod vedením vedoucího diplomové práce a s použitím odborné literatury a dalších informačních zdrojů, které jsou všechny citovány v práci a uvedeny v seznamu literatury na konci práce.

Jako autorka uvedené diplomové práce dále prohlašuji, že v souvislosti s vytvořením této diplomové práce jsem neporušila autorská práva třetích osob, zejména jsem nezasáhla nedovoleným způsobem do cizích autorských práv osobnostních a/nebo majetkových a jsem si plně vědoma následků porušení ustanovení § 11 a následujících zákona č. 121/2000 Sb., o právu autorském, o právech souvisejících s právem autorským a o změně některých zákonů (autorský zákon), ve znění pozdějších předpisů, včetně možných trestněprávních důsledků vyplývajících z ustanovení části druhé, hlavy VI. díl 4 Trestního zákoníku č. 40/2009 Sb.

V Brně dne ....

(podpis autora)

PODĚKOVÁNÍ

Děkuji vedoucímu diplomové práce Ing. Tomáši Potočňákovi za účinnou metodickou, pedagogickou a odbornou pomoc a další cenné rady při zpracování mé diplomové práce. Rovněž bych chtěla poděkovat společnosti FEI Česká Republika (část Thermo Fisher Scientifics) za příležitost spolupráce a poskytnutí dat.

V Brně dne ....

(podpis autora)

Contents

List of figures

List of tables

Introduction

Transmission electron microscopy is a technique able to image very small structures down to the atomic resolution. It is widely used in material science, biology, medicine and many other fields. Like most of the other digital images, the images obtained from the transmission electron microscope also suffer from distortion and noise caused during the imaging process. To obtain maximum of the information from the image, it is useful to reduce the noise using some filtrating method.

This work deals with the blind filtration of the images from transmission electron microscope. The first part contains basic description of the microscope and it mentions aberrations related to the lens system. In the second part, interactions between the specimen and electron beam are described, along with the review of several imaging techniques. The third part of this work is dedicated to the description of chosen image decomposition methods with focus of their application in image filtration. This part also includes a summary of chosen image quality assessment techniques.

The practical part includes the description of the algorithms for the implemented methods. Each method was firstly tested on model image and then it was applied on the whole image set. Obtained results are presented and commented in this part. The efficiency of filtration was assessed both objectively and subjectively. The median and averaging filter and filtering via image spectrum were used as commercial methods for comparison. In the end of the practical part, the results and applicability of all used methods are discussed. Conclusion brings propositions for the further analyses and improvement of implemented filtration methods.

1. Transmission electron microscope

The transmission electron microscope (TEM) is a device which enables the observation of very small structures down to the atomic levels. It was invented by Max Knoll and Ernst Ruska in Berlin between years 1931 and 1934. Unlike the light microscope the electron microscope uses the beam of very fast-moving electrons to form an image. The observed specimen is in a form of a very thin foil which should be electron transparent. Special type of TEM, using convergent beam to scan the image point by point, is called scanning transmission electron microscope (STEM).[24]

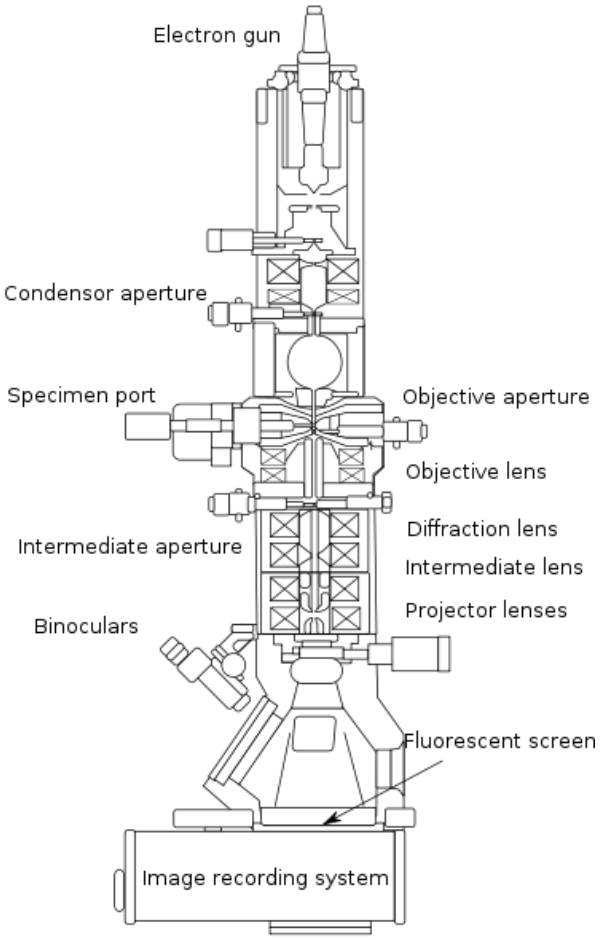

Fig. 1.: Transmission electron microscope - scheme [14]

1.1 Electron microscope components

The transmission electron microscope consists of several main components: control electronics, high voltage power supply, vacuum system, source of electrons, series of electromagnetic lenses, specimen holder, fluorescent screen and camera (Fig. 1).

The electron gun forms an electron beam; it is placed on the top of the microscope. The electron beam then goes through a system of the condenser lens which focuses the beam onto a specimen, where some electrons pass through and some are scattered or they interact with the specimen. A direct beam (the electrons that have passed through the specimen) then goes through a system of the objective lens, the intermediate lens and through the projective lens and falls onto a fluorescent screen. The vacuum system keeps the inside of the electron microscope clean from the gases and prevents the specimen from being contaminated. Those individual parts are described in the following paragraphs. [24]

1.2 Electron gun

The electron gun is characterized by a brightness B, which is a current I divided by the source area S and the solid angle Ω:

$$B = \frac{I}{S\Omega} \approx \frac{4I}{\pi^2 \alpha_0^2 d_z^2}, \tag{1.1}$$

where α_0 is the beam angle and d_z is the diameter of the electron source. There are more types of the electron guns which differ in the emission mechanism.

The electron guns with thermionic emission consist of three main parts. The electron beam is created in hot cathode and it is accelerated to the anode through the Wehnelt cylinder, which functions as an electrostatic lens. The materials used for cathode are usually tungsten or lanthanum hexaboride.

The field emission gun is another type of electron gun. The cathode is made from the tungsten in the shape of a sharp tip. Electrons are emitted by the phenomenon of quantum tunnelling with a strong electric field on the anode. Those guns can have very small virtual source diameter - from 5 to 30 nm, however they need to work under high ultravacuum, which is very expensive.

Cold field emission gun is very sensitive to the vibrations or magnetic fields. Very small source diameter can be reached when the emission tip is focused well using electric field and heat. This procedure has to be repeated after couple hours.

Electron guns working with thermionic field emission are more stable. The emission of electrons is caused by the electric field and it is stabilized using higher temperature (~ 1800 K). The emission current is increased using the Schottky effect which creates an electric field at the surface of the emitter and by that it lowers the local work-function. [24]

1.3 Magnetic lenses and their aberrations

The electron beam in the electron microscope is focused with magnetic lenses. Magnetic lens is a coil with copper windings and with casing and pole pieces made from magnetically soft iron. A focus effect of the lens is caused by the Lorentz force. Electron with an electric charge e and velocity $\boldsymbol{v}$ is affected by a strong magnetic field $\boldsymbol{B}$. Lorentz force is then:

$$\boldsymbol{F} = -e(\boldsymbol{v} \times \boldsymbol{B}). \tag{1.2}$$

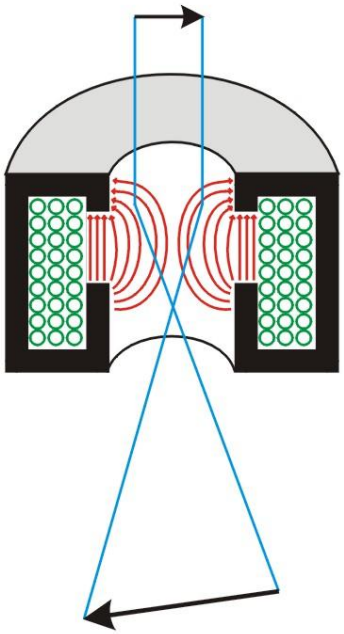

Fig. 2.: Magnetic lens [29]

An image from the magnetic lens is inverted and rotated. The rotation angle increases along with the current I. The focal length f of the magnetic lens changes with the current I. The resolution of electron microscope is determined by lens aberrations. Magnetic lenses can have more types of aberrations - spherical and chromatic aberrations, astigmatism and coma. [24] [45]

1.3.1 Spherical aberration

Spherical aberration causes that various electron beams focus on different focal points. This happens because the electrons which travel close to the edges of the magnetic lens are deflected closer to the optic axis than the other ones. Due to this aberration, a point source lying on the optic axis would be displayed as a circle of confusion. Spherical aberration is described by the spherical aberration coefficient C_S [mm] and it is approximately equal to the focal length of the microscope.

Theoretical resolution of the microscope then can be defined as δ:

$$\delta = 0{,}91(\, C_S\lambda^3)^{1/4}, \tag{1.3}$$

where λ is the wavelength of the electrons in the electron beam. According to this equation, better resolution can be reached by decreasing the coefficient C_S or by increasing the accelerating voltage, which leads to shorter wavelengths λ. A spherical aberration corrector has been developed recently, so the resolution of the tenth of a nanometer can be reached. [17] [24] [45] Spherical aberration of a single lens is presented in Fig. 3, where A, B, C represent incident beams and F_A, F_B and F_C are corresponding focal points.

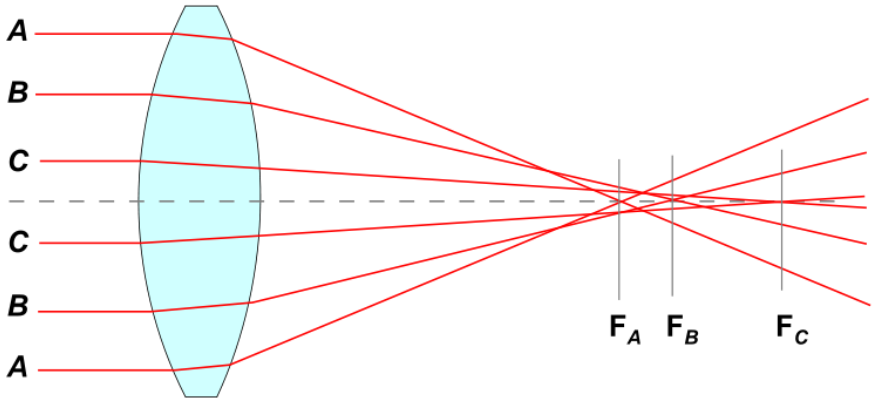

Fig. 3.: Spherical aberration [15]

The spherical aberration corrector is an objective lens system of a 200 kV TEM, able to correct not only spherical aberrations but also off-axis coma. This corrector consists of two electromagnetic hexapoles combined with four other lenses. The electron beam first falls onto a compound lens, then goes through the first round-lens doublet and continues through the first hexapole. Then it goes through the second doublet and finally through the second hexapole. The second hexapole compensates the primary aberrations of the first hexapole. Hexapoles cause a residual negative secondary aberration, which corrects the third-order spherical aberration of whole imaging system. [17]

1.3.2 Chromatic aberration

The electrons in electron beam can have different velocity, and those with higher velocity are less affected by the magnetic lens. This influences the focal length - a variation of the electron energy ΔE causes a variation of the focal length Δf. Due to differences of the focal length a point source is imaged as the circle of confusion. Energy changes can be caused by several reasons: fluctuations of the accelerating voltage ΔE, fluctuations of the current in the objective lens ΔI, fluctuations of the initial velocity of the electrons ΔV when leaving the cathode and energy losses caused by the transmission through the specimen. When not considering the energy losses on the specimen, changes in the focal length Δf can be described as

$$\Delta f = C_C \left[\left(\frac{\Delta V}{V} \right)^2 + \left(\frac{2\Delta I}{I} \right)^2 + \left(\frac{\Delta E}{E_0} \right)^2 \right]^{1/2}, \tag{1.4}$$

where C_C [mm] is the chromatic aberration coefficient, which is also approximately equal to the focal length f.

Nowadays the accelerating voltage and the current have only little fluctuations, however the energy losses on the specimen are not negligible. The influence of the chromatic aberration increases with the thickness of the foil specimen. Non-elastically scattered electrons can be eliminated by using the energy filter. [24] [45]

1.3.3 Astigmatism

This aberration is also related to the focal length. The two different electron rays perpendicular to each other, both of them propagating along the optic axis, each one of them have a different focal length. The distance of those focal points is marked with Δf_α and its length is in the order of micrometers. Astigmatism can be caused by the imperfections of the pole-pieces construction or by the heterogeneity of their material. Ferromagnetic specimen can also be one of the causes. There can be more types of astigmatism - the most common is the two-fold astigmatism but also three-fold or four-fold astigmatism can be observed. Astigmatism can be corrected using a magnetic field with elliptical symmetry. Its intensity is controlled by quadrupole coils called the stigmators. When using camera and computer for imaging, astigmatism can be eliminated in real time by the Fourier transform. [24]

1.3.4 Coma

This aberration can appear when the specimen is being illuminated by the off axis incident beam. A point source placed in the object plane is then projected to the image plane with deformation in a shape of comet. This artifact is formed by the different phase shift of the diffracted beams. Correction can be realized by the deflection coils. [24]

1.4 Lens systems

As mentioned above, the electron microscope has more lens system. The main purpose of the condenser lens is to regulate the intensity and the aperture angle of the electron beam. The objective plays the main role of the whole microscope, because its properties determine the resolution. The purpose of this lens system is to form an image of the specimen. Objective lens can have its upper and lower pole-pieces separated, each one having its own coil. In the gap between both pole-pieces the specimen and the objective aperture are inserted. This type of lens is very useful in STEM mode. The projector lens system then projects and magnifies the image on the screen or photographic material. [24] [39] [45]

1.5 Apertures

In the electron microscope there are several different apertures. Their diameters vary from 10 to 300 μm and their thickness is usually between 25 and 50 μm. The condenser aperture limits the angle of the electron beam hitting the specimen. The objective aperture is placed in the objective focal plane. By the choice of its size the type and the quality of the contrast is determined. Objective aperture with diameter between 10 to 30 μm is used to choose direct or diffracted beam, larger aperture with diameter between 200 to 300 μm allows more rays to go through. The selected area aperture is placed behind the objective aperture, in the objective image plane. This aperture determines the size of the diffracting area. [24]

1.6 Vacuum system

The vacuum system keeps the pressure inside the electron microscope on the required values and it prevents the specimen from contamination. One microscope typically employs more different vacuum pumps. Pressure value is usually kept on the order of 10^{-5} Pa, where higher or lower vacuum levels can be required in different areas.

Initially the microscope is evacuated to a rough vacuum level using rotary vane pump or scroll pump. Both of them are reliable, however the scroll pump does not need oil cooling and lubrication which makes it preferred nowadays. Diffusion pump is used for evacuation to low or high vacuum level. Because it traps air molecules by oil vapors, it can contaminate evacuated space. A cold trap can be placed near the outlet of diffusion pump to prevent the oil from backstreaming. Ion-getter pumps produce ultra-high vacuum but they can be operated effectively only when initial vacuum level is at least around 10^{-3} Pa. They are quite small and do not need cooling thus they are usually placed close to the specimen holder or the electron gun. [24]

1.7 Electron detection and display

Human sight is not adapted to see electrons so they have to be converted to a visible light. In TEM a fluorescent viewing screen with ZnS coating is employed. For image forming more approaches are available; either the image can be formed digitally or the photographic film can be used. [24] [39]

Besides the fluorescent screen there are other electron detectors: semiconductor detectors and scintillator-photomultiplier systems. In semiconductor detector incoming electrons are converted to a current. This detector is quite responsive and can be cut into any shape. A scintillator is a component which converts electrons to a visible light. Different materials provide different decay times - for ZnS decay time is in the order of μs, Ce-doped yttrium-aluminum garnet (YAG) has decay time in the order of ns. Light obtained from the scintillator is then amplified by the photomultiplier. Scintillators can have an aluminium coat to eliminate the visible light. [39]

Almost real-time observation can be realized via charge-coupled device (CCD). It consists of the YAG scintillator connected to the phototransistor array. CCD is usually placed under the fluorescent screen. [24]

1.8 Parameters of the electron microscope

Quality of the imaging process can be characterized by many parameters. Some of them are described in the following paragraphs.

1.8.1 Resolution

The term resolution in electron microscopy means the "minimum resolvable distance" in the specimen. In the TEM mode the resolution is connected to the properties of the objective, in the STEM mode the resolution depends on the beam diameter. When assuming there are no aberrations, the theoretical resolution is described by the Rayleigh criterion. A single point source is always imaged as the Airy disk even when the aberrations are absent. When the maximum of one source and first minimum of the other source lie upon each other, the eye can distinguish resulting image as two overlapping sources. Theoretical resolution r_{th} is then defined as

$$r_{th} = 0.61 \frac{\lambda}{\beta}, \tag{1.5}$$

where λ is the wavelength and β is the semiangle of collection of lens. Practically the resolution is affected by the lens aberrations which were described in the previous paragraphs. [24] [39]

1.8.2 Depth of focus, depth of field

The parameter depth of focus, D_{im}, is related to the image plane. It defines the distance along the optic axis on the both sides of the image plane - above and below it- where the image is still sharp. The depth of field, D_{ob}, is the parameter of the object plane. D_{ob} describes the range of the specimen movement along the optic axis without losing the sharpness in the image. The specimen can be moved in both directions along the optic axis. [39]

1.8.3 Magnification

Magnification *M* and demagnification *1/M* in TEM is operated by the changes in magnetic lens strength. Stronger lens has longer focal length. Assuming that the distance of the object (specimen) from the lens stays unchanged, the distance of the image from the same lens shortens and results in smaller magnification. It means that in TEM strong lens are used for demagnification and weak lens are used for magnification, which is opposite to the light microscope. To obtain greater magnification several weak lenses are employed in tandem. [39]

2. Interaction of the electrons with the specimen

When the electron beam comes across the specimen several interactions can occur. Those interactions will be described in the following paragraphs.

The primary electron beam which is created in the electron gun and hits the specimen is called the incident beam. The electrons which are scattered by the interaction with the specimen are either called the direct beam, when they travel parallel to the incident beam, or the scattered beam if they are scattered at any non-zero angle. Either the electrons are scattered or unaffected by the specimen. This interaction causes changes in the intensity of the beam. This nonuniform distribution of electrons carries all the information about the specimen. [39]

2.1 Electron scattering

Electrons can be scattered either elastically or inelastically. In the first case the interaction leads to the direction change with negligible energy losses, in the second case some measurable loss of energy occurs. Next the scattering can be divided to coherent and incoherent. The incident beam is assumed as coherent, which means that its electron waves are in phase and of the same wavelength. Coherently scattered beams then have their electrons in phase just like the incident beam, unlike the incoherently scattered beams whose electrons have no phase relationship. Usually elastically scattered electrons are coherent and inelastically scattered ones are incoherent. [24] [39]

Interaction with the thin specimen can result either in forward scattering or backscattering. If the beam is scattered through the angle smaller than 90°, then it is forward scattering, otherwise it is backscattering. On a bulk specimen the incident beam is only backscattered. In the TEM most information is obtained from the forward scattered electrons, which include elastic and inelastic scattering, Bragg scattering, diffraction and refraction. Electron can be scattered only once (single scattering) or more times (plural scattering ≤ 20 times, multiple scattering > 20 times). [39]

Elastic scattering is caused by the interaction of the electrons with the electrostatic potential of atomic nuclei. Electron changes its direction and the angle θ of the change is usually very small. It means that small direction changes ($\theta \sim 10$ mrad) does not affect the coherency of the beam. Thus, scattering through larger angles (more than 30 mrad) is the incoherent elastic scattering. Inelastically scattered electron gives its energy either to the atom or to the whole crystal. Due to the energy, transfer electrons from the specimen are excited. This can increase the temperature of the specimen, its radiation damage or secondary deexcitation processes - X-ray photons emission, Auger electrons emission, cathodoluminescence. [24]

2.2 Wave-particle duality

Electrons can act as a particle and as a wave too. The proof of the wave character is the diffraction, an example of the particle character is typically the photoelectric effect. The particle with the mass *m* and velocity *v* has wavelength λ:

$$\lambda = \frac{h}{mv}, \tag{2.1}$$

where *h* marks the Planck constant. The product of *m* and *v* is called momentum and its mark is *p*. [24]

2.3 Cross section

The cross section is a parameter describing the chance of a particular electron to interact somehow with an atom. For every possible interaction there is a different cross section *Q* dependent on the beam energy. Its unit of area is barn (1 barn = 10^{-24} cm^2). Cross section divided by the actual area of the atom represents a probability of the occurrence of a scattering event. Considering that the specimen consists of *N* atoms and regarding the cross section as the number of scattering events per distance unit, the probability of scattering on a specimen of the thickness *t* is defined as:

$$Q_T t = \frac{N_0 \sigma_T (\rho t)}{A}; \tag{2.2}$$

where N_0 is Avogadro's number, *A* is the atomic weight of the specimen atoms, ρ is the specimen density and σ_T represents the total scattering cross section of an isolated atom. [39]

2.4 Mean free path

A distance which the electron travels between two interactions, called the mean free path, can be also used to describe total cross section. An inverse value of this parameter is the average distance between two scattering events. Mean free path λ is defined as:

$$\lambda = \frac{1}{Q} = \frac{A}{N_0 \sigma_T \rho}; \tag{2.3}$$

This parameter can be used to determine the thickness of the specimen so that the plural scattering is avoided. [39]

2.5 Differential cross section

By this parameter the angular distribution of scattering is described. The differential cross section is marked $d\sigma/d\Omega$ and it is defined as:

$$\frac{d\sigma}{d\Omega} = \frac{1}{2\pi \sin\theta} \frac{d\sigma}{d\theta}; \tag{2.4}$$

where θ marks the angle through which the electrons are scattered and Ω is the solid angle into which they scatter. The relationship between θ and Ω is

$$\Omega = 2\pi \sin\theta \, d\theta. \tag{2.5}$$

By integrating the equation (2.4) the definition of the cross section for scattering into angles greater than θ is obtained: [39]

$$\sigma_\theta = \int_\theta^\pi d\sigma = \int_\theta^\pi \frac{d\sigma}{d\Omega} sin\theta \, d\theta. \tag{2.6}$$

2.6 Diffraction

The diffraction is one of the most important phenomenon related to the interactions of the electrons and the matter in the TEM. The diffraction pattern (DP) provides information about the specimen such as its shape, chemical and crystal structure or information about the lattice. [39] In the following paragraphs the basic principles of diffraction will be given and some diffraction techniques will be described.

2.6.1 Diffraction in light optics

In the light optics the diffraction is a phenomenon that occurs when a light wave interacts either with a very small aperture or slit, comparable to the wavelength, or with an obstacle. The wave is bended around the aperture and spreads behind it. The smaller the aperture, the more the wave bends. According to the Huygens principle every point on a waveform is a source of spherical wavelets so the slit functions as a generator of new wavelets.

The diffraction pattern is typically formed from light and dark stripes - an interference maxima and minima. When the aperture is in the circular shape the diffraction pattern is composed of several concentric rings with central disk. In the case of the diffraction on two or more slits the wavelets interfere witch each other. The resultant interference maxima are very thin, thus they are called interference lines. [19]

2.6.2 Electron diffraction

In the TEM the diffraction occurs when the electron beam waves interact with the atoms in the specimen. The wavelength of electrons in the beam has to be approximately the same as the distance between atoms in the specimen. Secondary spherical wavelets created by diffraction interfere with each other, where the interference can be either destructive or constructive. Under certain conditions the constructive interferences produce diffracted beams. [24] [40]

2.7 Imaging in transmission electron microscope

The TEM specimen observation result can be either a diffraction pattern (angular distribution) or a direct specimen image (spatial distribution). Selection between these two is realized by the setting of the lenses and apertures. The diffraction pattern is formed when the back focal plane of the objective acts as the object plane of the intermediate lens. To form the specimen image on the viewing screen the object plane of the intermediate lens has to be the objective image plane. Usually the diffraction pattern is viewed first and then the contrast mechanism is chosen. [39] [40]

Contrast

Electron intensity which is originally uniform in the incident beam becomes uneven after the interaction with the specimen. To obtain applicable image with good contrast some electrons have to be eliminated from imaging using the objective aperture. Contrast mechanism is chosen by the microscope operator and it depends on many factors like tilt and thickness of the specimen, beam convergence or size of used apertures. Contrast *C* is defined as:

$$C = \frac{I_2 - I_1}{I_2} = \frac{\Delta I}{I_2}, \tag{2.7}$$

where I_1 and I_2 are intensities of two adjacent image areas. [24] [41]

2.8 Diffraction imaging techniques

As mentioned above, the result of the diffraction imaging is the diffraction pattern. It is usually used to chose the technique for contrast imaging. Some diffraction imaging techniques will be described in the following paragraphs. [40]

2.8.1 Selected area diffraction

The selected area diffraction (SAD) imaging is a technique where the illuminated area of the specimen is reduced using a selecting aperture. This aperture is inserted in an objective image plane so the virtual aperture at the specimen plane is created. Whole specimen or its large area is illuminated by a parallel beam, however any electron falling outside the defined area will not participate to the forming of the diffraction pattern. The diameter of the incident beam is usually approximately from 1 to 10 μm. The SAD pattern is in a form of sharply focused spot marks (Fig. 4). [39] [40]

Fig. 4.: Selected area diffraction pattern [31]

2.8.2 Convergent-beam electron diffraction

Convergent-beam electron diffraction (CBED) is another technique using only small area of the specimen to form the diffraction pattern. The difference between SAD imaging and CBED is that the CBED actually uses small incident beam to illuminate the specimen. The limitation to the beam is realized by converging it so smaller beam diameter is achievable, usually the diameter is approximately between 10 and 100 nm. There are more types of CBED - they differ in the convergence semiangle α, which is defined by the choice of the condenser aperture C2. The term microdiffraction is used for $2\alpha \sim 0{,}01°$, classical CBED has the range of 2α from 0,1°to 1° and when the angle is between 2 and 6° the method is called large angle convergent beam electron diffraction (LACBED). The diffraction pattern is formed by disks (Fig. 5) which vary in the size, dependent on the α. If the disks in DP do not overlap, then it is called a Kossel-Möllenstedt pattern; otherwise the term Kossel pattern is used.

The CBED imaging can be affected by the contamination of the specimen, on the other hand the specimen can be damaged by the heat. CBED is used to provide information about the thickness of the specimen, the lattice parameters, determination of the crystal symmetry of the crystal defect. [24] [39] [40]

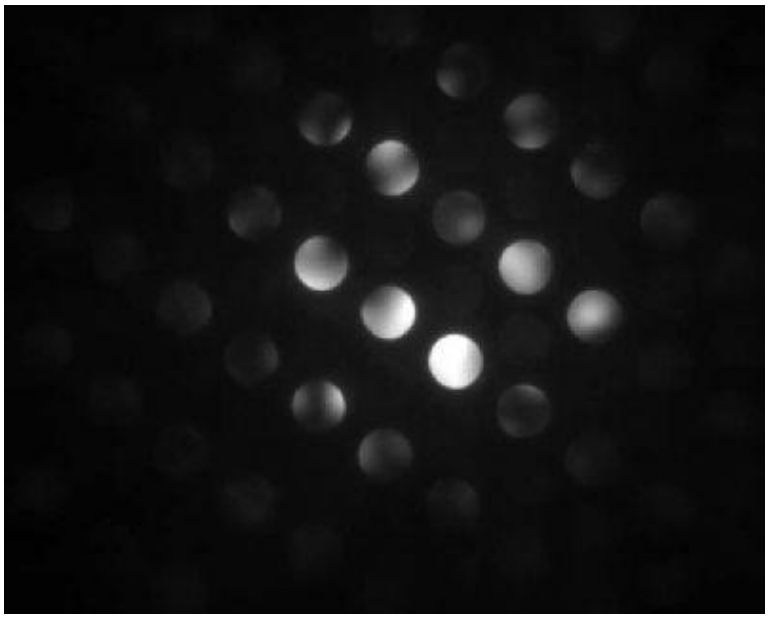

Fig. 5.: Convergent beam diffraction pattern [11]

2.8.3 Other diffraction imaging techniques

Besides the SAD and CBED techniques there are more imaging techniques using diffraction. The double diffraction phenomenon means that the beam that was already diffracted is rediffracted again. This can happen when the specimen is a two-phase material. Double diffraction can produce extra marks in the diffraction pattern or it can increase the intensity of real reflection marks. The precession electron diffraction (PED) was originally designed for an X-ray diffraction. The incident beam is tilted by the coils and it rotates around the axis parallel to the optic axis with the usual frequency equal to 50 Hz. The resultant diffraction pattern is formed by the summation of all the patterns obtained from every beam tilt. [24] [40]

2.9 Contrast imaging techniques

Three elementary types of contrast are used in TEM imaging:

- amplitude contrast (mass-thickness contrast, diffraction contrast);
- phase contrast;
- Z contrast. [24]

2.9.1 Bright-field and dark-field

An objective aperture inserted into the back focal objective plane determines whether the direct beam or the diffracted beam will form the image. A bright-field (BF) image is formed when the direct beam is chosen. If any diffracted beam is chosen, the obtained image is called a dark-field (DF) image. An example of both imaging techniques is in the Fig. 6, both images are from the Thermo Fisher Scientifics. In DF imaging the selected beam is off-axis so the imaging process can be affected by the lens aberrations. Thus, the DF image cannot be focused properly due to adjusting the lens. This can be avoided by tilting of the incident beam hitting the specimen. The tilt angle has to be equal and opposite to the angle of the diffracted beam. Selected beam then travels along the optic axis. This method is called centered dark-field (CDF) imaging. [39]

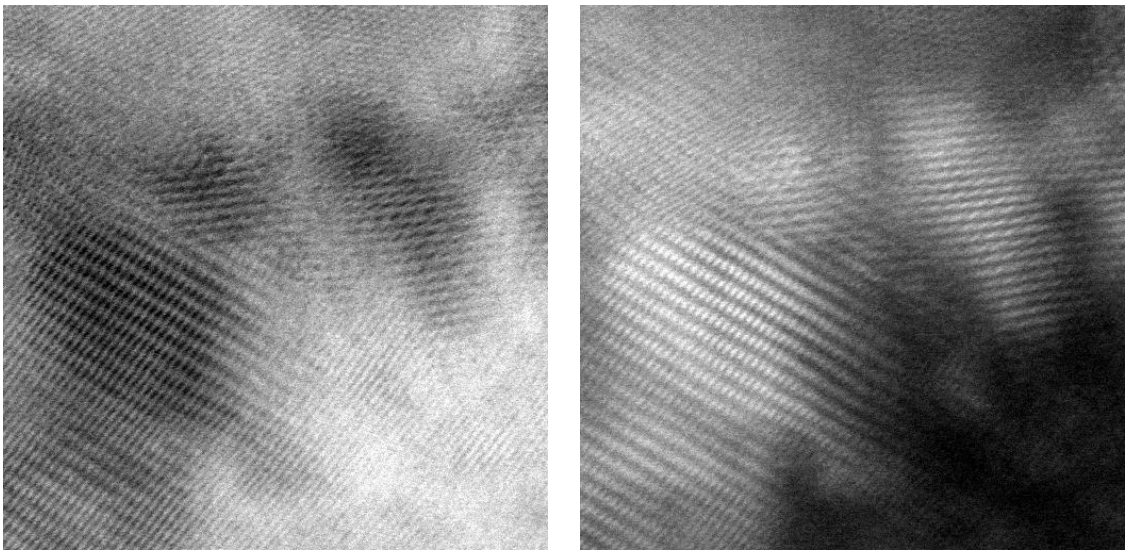

Fig. 6.: Example of the BF image (left) and the DF image (right)

2.9.2 Amplitude mass-thickness contrast

This imaging technique is dependent on the thickness and the density (atomic number *Z*) of the specimen. The elements with higher *Z* scatter more electrons than those with lower *Z*. Assuming that the specimen is of the same thickness, high-mass (high *Z*) parts of the specimen will cause more scattering interactions than parts that contain elements with lower *Z*-number. That also means that specimen with homogeneous distribution of the parameter *Z* will scatter more electrons by its thicker part than by its thinner part. Those off-axis scattered electrons are then eliminated by the objective aperture so in the bright field imaging the thicker regions of the regions with higher *Z* will be dark while thinner regions (lower *Z*) will be bright. The mass-thickness contrast is used for noncrystalline materials observation - polymers and biological specimens. [24] [41]

2.9.3 Amplitude diffraction contrast

In TEM diffraction contrast imaging, the image is formed by coherent elastic scattering. Diffraction occurs only at specific angles (Bragg angles) so the specimen has to be tilted correctly which usually takes a lot of time. If too many electrons are scattered, the intensity of the direct beam is very low and obtained BF image is quite dark. This problem can be solved by tilting the specimen to two-beam conditions. In this case there is only one strong diffracted beam and direct beam. In this technique two other different modes can be used - weak-beam imaging or strong-beam imaging, which are chosen by tilting the incident beam.[24] [41]

The weak-beam microscopy is contrast imaging method which is realized either in the bright-field or in the dark-field. Weak-beam dark-field (WBDF) imaging is widely used because under certain conditions it gives very strong contrast. It is suitable for dislocations observation. [41]

2.9.4 Phase contrast

Unlike the imaging techniques which are mentioned above, the phase contrast imaging uses more beams to form an image. Phase (interference) contrast is used in the atomic resolution imaging techniques. Large objective aperture allows more beams to pass through; those beams interfere with each other and form the image. The objective has to be defocused because diffracted beams are phase shifted and this defocus compensates the phase difference. [24] [41]

2.10 High resolution imaging

High resolution TEM (HRTEM) imaging is related to high spatial frequencies, i.e. small distances in the scene. In the diffraction pattern the points which are distant from the optic axis correspond to high spatial frequencies. That is caused by the spherical aberration of the objective lens. Thus, each point of the specimen is always imaged as a disk in the image. Consequently, each point in the final image is formed from many points in the scene - specimen. The relationship between the specimen function $f(\boldsymbol{r})$ and the intensity of the corresponding place in the image $g(\boldsymbol{r})$ is described as:

$$g(\boldsymbol{r}) = \int f(\boldsymbol{r}')h(\boldsymbol{r}-\boldsymbol{r}')dr' = f(\boldsymbol{r}) \otimes h(\boldsymbol{r}-\boldsymbol{r}'), \tag{2.8}$$

where $\boldsymbol{r}$ represents the lattice vector and $h(\boldsymbol{r})$ is called the point-spread function. In reciprocal space this relationship is expressed as:

$$G(\boldsymbol{u}) = H(\boldsymbol{u})F(\boldsymbol{u}), \tag{2.9}$$

with $\boldsymbol{u}$ being a reciprocal-lattice vector and $G(\boldsymbol{u})$, $H(\boldsymbol{u})$ and $F(\boldsymbol{u})$ being the Fourier transform of $g(\boldsymbol{r})$, $h(\boldsymbol{r})$ and $f(\boldsymbol{r})$, respectively. Now $H(\boldsymbol{u})$ is called the contrast transfer function (CTF) and it expresses the transference of the contrast between $\boldsymbol{u}$ space and image. Contrast transfer function is affected by multiple factors:

$$H(\boldsymbol{u}) = A(\boldsymbol{u})E(\boldsymbol{u})B(\boldsymbol{u}). \tag{2.10}$$

$A(\boldsymbol{u})$ stands for the aperture function which says that spatial frequencies greater than value determined by the aperture radius are eliminated. $E(\boldsymbol{u})$ is the envelope function, related to the attenuation of the wave. The last function in the equation, $B(\boldsymbol{u})$, is the aberration function.

The specimen function ***f(r)*** is also called specimen transmission function. To describe the specimen, some models were implemented. Very thin specimens can be modeled using the weak-phase-object approximation (WPOA), with the equation:

$$f(x,y) = 1 - i\sigma V_t(x,y), \tag{2.11}$$

where V_t is the potential of the specimen with thickness t and σ is the interaction constant. Another function related to the imaging process is transfer function ***T(u)***, defined as:

$$T(\boldsymbol{u}) = A(\boldsymbol{u})E(\boldsymbol{u})2sin\chi(\boldsymbol{u}), \tag{2.12}$$

where ***χ(u)*** is called the phase-distortion function. For incoherent illumination, ***T(u)*** and ***H(u)*** are equal. The value of ***T(u)*** determines the type of contrast. Negative ***T(u)*** indicates that the diffracted beam is phase-shifted by -π/2 which results in positive phase contrast - dark atoms against bright background. On the other hand, positive value of ***T(u)*** means phase-shift of the diffracted beam by +π/2, resulting in negative phase contrast. Then atoms are bright against dark background. [41]

The point resolution for HRTEM is defined as:

$$r_{Sch} = 0{,}66\, C_s^{\frac{1}{4}} \lambda^{\frac{3}{4}}, \tag{2.13}$$

and it is related to the Scherzer defocus:

$$\Delta f_{Sch} = -1{,}2(C_s\lambda)^{\frac{1}{2}}. \tag{2.14}$$

The resolution corresponds to the first zero crossing of the transfer function at Scherzer defocus. [13] [41]

2.11 Other imaging techniques

Besides the imaging techniques described above there are other techniques used in the TEM. Lorentz microscopy is a form of the phase contrast imaging and it is used for the observation of the magnetic specimens. Electron holography was originally proposed to improve the resolution. It allows to record both the amplitude and the phase of the transmitted beam and to reconstruct the object as a hologram without deformation caused by the aberrations. *In situ* microscopy is technique where dynamic changes in microstructure are observed in real time. In cryo-electron microscopy the specimen is observed at liquid nitrogen temperatures. It is used to study biological specimens in their native environment. The electron tomography is also possible. The specimen is tilted through defined angles (this requires special specimen holder) and the resultant 3D structure is obtained using computer reconstruction algorithms. [24] [41]

2.12 Scanning transmission electron microscope

Scanning transmission electron microscope (STEM) is a special type of the TEM. The STEM uses convergent electron beam which is moving within a rectangular frame. The image is formed point by point as the specimen is scanned. Unlike the TEM, this microscope has extra additional coils - scanning coils which manage the movement of the beam. The observation of the resultant image is realized via computer monitor, the imaging on the fluorescent screen is not possible. STEM employs several different detectors:

- bright field (BF) detector is used to detect the intensity of the direct beam;
- annular dark field (ADF) detector registers the diffracted beams;
- high annular dark field (HAADF) detector collects the information from the electrons scattered through large angles.

Today's TEMs can usually work in both modes - conventional transmission electron microscopy and scanning transmission electron microscopy too. [24]

2.13 Imaging in scanning transmission electron microscopy

The incident beam in the STEM imaging has to be parallel to the optic axis. For this purpose, the scan coils are employed. In STEM the CBED pattern can be observed too. It is formed in the back focal objective plane and it is static. If the beam is stopped from scanning, CBED pattern can be projected on the fluorescent screen. As there are no lenses used to form an image, the resolution is not affected by the chromatic aberration. The image is formed simultaneously with the specimen being scanned. Signal obtained from the specimen is detected, amplified, and it is displayed on the corresponding place on the CRT (cathode ray tube). It takes from seconds to minutes to form an image. [39]

2.13.1 Bright-field and dark-field in STEM

In STEM there are no apertures used to chose the required beam that forms an image. The choice of the beam is realized by the choice of the detector. For bright-field imaging the BF detector is inserted into the direct beam so all the other electrons are excluded from the image forming. The detector is usually placed in the plane of diffraction pattern. To obtain an DF image either the BF detector or special detectors can be used. For the first approach the stationary diffraction pattern is shifted so that the required scattered beam is on the optic axis. Then this beam is detected on the BF detector. Usually the second approach is employed. [39]

The BF detector is surrounded by the annular dark-field (ADF) detector. The ADF detector register scattered electrons which contribute to the image. Around the ADF detector there is another one - high-angle annular dark field (HAADF) detector. It serves to detect electrons scattered through high angles. [39] [40]

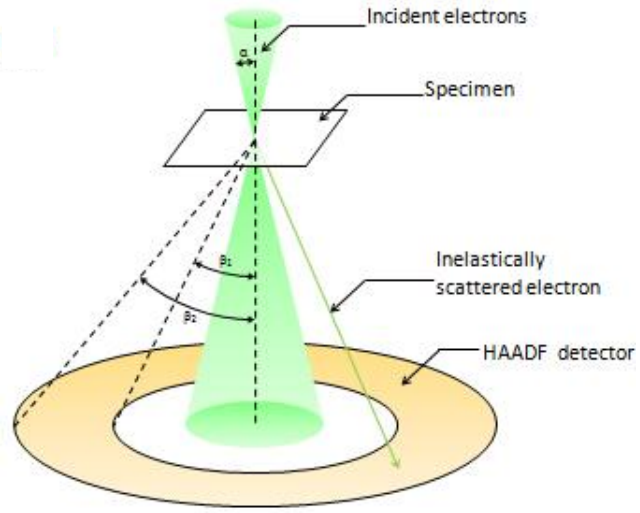

Fig. 7.: HAADF STEM ray diagram [5], modified

2.13.2 Z-contrast

Z-contrast belongs to the HRTEM imaging techniques. Specimen is scanned point by point with convergent electron beam and the image is observed only on the computer. The resolution is determined by the diameter of the beam, typically the diameter can be about 0,2 nm but 0,05 nm is achievable with the spherical aberration corrector.

The image is formed only from the contributions of the incoherently scattered electrons, which were scattered through the semiangles larger than 50 mrad. To avoid the detection of Bragg electrons a special detector is employed - high angle annular dark field (HAADF) detector. Electron scattered through lower angles can also contribute to the obtained information when using special detectors. Local chemical structures can be determined using the electron energy loss spectrometry (EELS) and the energy dispersive X-ray spectroscopy (EDS). [24] [41]

3. Transmission electron microscope image filtering

Like all other imaging techniques, the TEM imaging also deals with the noise and blur in the images. The noise can originate during the image acquisition, during the transmission process or within the signal registration. [26] In the following paragraphs several basic filtering techniques are described and then chosen blind filtration techniques based on the image decomposition are proposed.

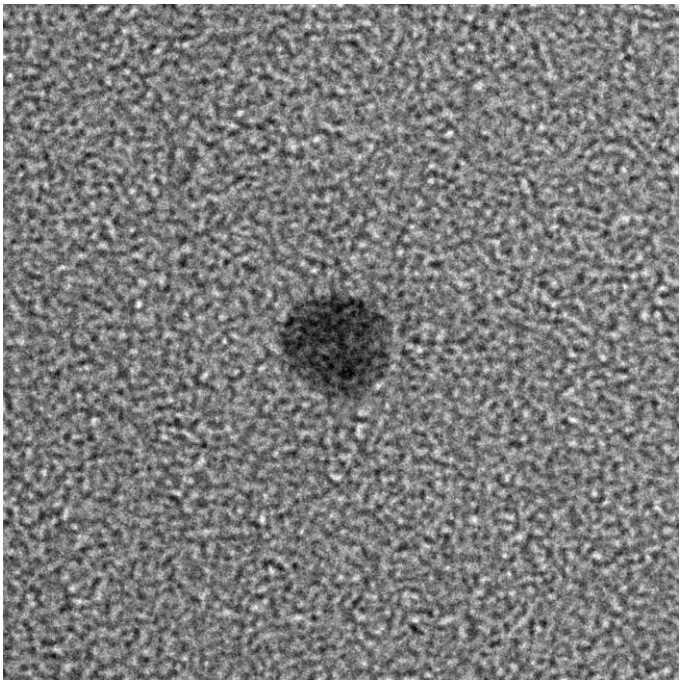

Fig. 8.: TEM image before filtration

3.1 Basic filtering methods

In [26] three filtering methods for TEM images are described. All proposed methods were applied to the TEM image of cadmium sulfide nanoparticles with amplifier (Gaussian noise). The first two methods are the Mean (or average) filter and the Median filter. Both of them use the mask which is moving upon the image and for each pixel its new (filtered) value is computed from the pixels from its neighborhood, defined by the size of the mask. The Mean filter is linear filter, and, as its name says, the output pixel value is computed as mean value of the pixels in the mask. This filter is not good at preserving the edges in the image.

The Median filter is an example of non-linear filtering; the output pixel value is defined as the median value of the pixels in the mask. Its major advantage is that it is able to reduce the noise without damaging the edges. The third method proposed in [26] is the Wiener filter, which is a linear FIR filter, widely used for the filtration of one-dimensional and two-dimensional data. However, this filter assumes the knowledge of the noise's spectral characteristics, which does not correspond with the idea of the blind filtration.

3.2 Blind deconvolution

The blind deconvolution is widely used for the image filtration. This method assumes that the blur in the image is caused by spatially invariant point spread function (PSF). Considering this assumption an observed (blurred) image *G* can be expressed as the convolution of the PSF (marked *H*) and the original image *F*. [42]

The paper [25] gives the description of two approaches to the blind image deconvolution. In the first approach the PSF and the original image are estimated separately. This involves a priori identification techniques. The second approach is characterized by the simultaneous estimation of both, the PSF and original image, in one complex algorithm. An example of this approach can be blind deconvolution using modeling to estimate the parameters. The blurred image is considered to be an autoregressive moving average (ARMA) process, with the original image being the autoregressive part and the PSF being the moving average process.

In the paper [42] the polynomial computations are proposed for the blind deconvolution. The blurred image *G* is regarded as the convolution of the original image *F* with PSF (*H*) with addition of noise *N*. Also, the basic description of four MATLAB blind deconvolution functions is given there. Results of the proposed method are compared with the results obtained using these four functions. [42]. Though the blind deconvolution is quite popular method for blind image filtering, it is not the topic of this work.

3.3 Empirical mode decomposition

The empirical mode decomposition (EMD), proposed in [20], is a method suitable for the decomposition of the non-stationary and non-linear data. The result of EMD is the input data being decomposed to a set of intrinsic mode functions (IMFs) and a residue, which is a part of the data that cannot be decomposed, i.e. the trend.

The IMF has to fulfill two conditions: The number of extrema (local minima and local maxima) and the number of zero-crossings in the data either has to be equal or differ at most by one; and at any point the mean value of the upper envelope and the lower envelope is zero. [20]. The EMD offers many advantages - it is an adaptive method that analyzes data on the basis of their local characteristics, thus, it can effectively detect nonlinearities and nonstationary oscillations. Applied to the white noise the EMD functions as a dyadic filter bank. On the other hand, intermittent data can cause the mode mixing. [43]

3.3.1 Bi-dimensional empirical mode decomposition

Bi-dimensional empirical mode decomposition (BEMD) is a variation of 1D EMD adapted for the image decomposition.[16] The description below is taken from the paper [7]. The original image *I(i,j)* with the dimensions *M* and *N*, serves as the first input to the BEMD:

$$input_{lk}(i,j) = I(i,j), \tag{3.1}$$

where *l* is the index of IMF, *k* is the index of the current step and *i*, *j* are spatial coordinates. The procedure consists of several steps. First in the input image all the local maxima and minima are found. 2D spline interpolation is used to form the upper envelope $e_{max}(i, j)$ from the local maxima, and the lower envelope $e_{min}(i, j)$ from the local minima. When both envelopes are determined, their mean is computed:

$$e_{mean_{lk}}(i,j) = \frac{e_{max}(i,j) + e_{min}(i,j)}{2}. \tag{3.2}$$

Mean envelope is subtracted from the input image, the difference is marked $h_{lk}(i,j)$. After the difference is obtained, the stopping criterion is computed as:

$$eps = \frac{\sum_{i=1}^{H}\sum_{j=1}^{W}\left|e_{mean_{lk}}(i,j)\right|}{M \times N}. \tag{3.3}$$

The *eps* is compared to the threshold τ and if it satisfies the condition $eps < \tau$, then the component $h_{lk}(i,j)$ is considered as $IMF_l(i,j)$. If not, the current $h_{lk}(i,j)$ is considered as $input_{l(k+1)}(i,j)$ and the process is repeated. When the $IMF_l(i,j)$ is obtained, the image residue $R_l(i,j)$ is computed as:

$$R_l(i,j) = input_{lk}(i,j) - IMF_l(i,j) \tag{3.4}$$

The two situations can occur when obtaining the residue. In the first case the residue becomes the new input. In the second case there are no more local maxima or minima and whole EMD process is terminated. Then the original image can be expressed as:

$$I(i,j) = R_l(i,j) + \sum_{l=1}^{L} IMF_l(i,j). \tag{3.5}$$

In the paper [7] the EMD was proposed to enhance the underwater RGB images.

The paper [16] presents two ways of the definition of extrema in the image. The input image is described as *I(i, j)* with *i, j* being the discrete spatial coordinates. For *p(i, j)* the condition is that $p(i,j) \in \Omega_{(i,j)}$, $\Omega_{(i,j)}$ being the set of eight neighboring pixels to the pixel with coordinates *i, j*. Extrema can be defined as:

$$I(i,j) = \begin{cases} maximum\ if\ I(i,j) > p(i,j) \\ minimum\ if\ I(i,j) < p(i,j) \end{cases} \tag{3.6}$$

or

$$I(i,j) = \begin{cases} maximum\ if\ I(i,j) \geq p(i,j) \\ minimum\ if\ I(i,j) \leq p(i,j) \end{cases}. \tag{3.7}$$

The first equation is called the general extrema identification mode, the second one is the structural extrema identification mode.

Several approaches to the 2D interpolation can be used. The paper [7] mentions the 2D spline interpolation, in the paper [16] the trigonometric interpolation function is applied. In the paper [4], BEMD employs the green's function for the envelope surface interpolation. Their method is called Green's function in tension-based BEMD (GiT-BEMD). In [3] the GiT-BEMD was used for the analysis of fMRI images.

3.3.2 Ensemble empirical mode decomposition

Although the EMD is very useful tool, it still deals with some drawbacks. Its major problem, as mentioned above, is the mode mixing, related to the intermittent signals. The ensemble empirical mode decomposition (EEMD) proposed in [43] brings a solution in the addition of the white noise, which makes it a noise-assisted data analysis (NADA) method. Its principle is to add white noise to the signal before the beginning of the sifting process. Multiple trials are made and in the end white noise is eliminated by averaging process of the corresponding IMFs.

The white noise appears uniformly in whole time-frequency space. When added to the signal, white noise automatically adjusts different scales in the signal to proper scale defined by the noise. If only one realization of noise-assisted decomposition was used, the obtained results would be very noisy. That is the reason why multiple trials are made and the final result is calculated as their mean.

A single observation is multiplied and to each "new" observation different realization of white noise is added. This basically leads to *i* different observations. The EMD is applied to each of these observations to decompose them into IMFs. Finally, the ensemble means of the corresponding IMFs are calculated. Thanks to the number of trials the white noise eliminates itself. [43]

3.3.3 Multi-dimensional ensemble empirical mode decomposition

The EEMD method proposed in [43] was originally applied to one dimensional data. For the decomposition of multidimensional data its variation was proposed - the multi-dimensional ensemble empirical mode decomposition (MDEEMD). The principle described below (taken from [10]) deals with two-dimensional data but it can be implemented on multi-dimensional data easily.

The input for the MDEEMD is matrix *I* with the size *(i, j)*. The EEMD is firstly applied in only one direction of *I*, for example horizontal direction - the rows. All rows individually are decomposed into *m* components. Components of the corresponding level *m* are collected to the matrix *RX(m, i, j)*, thus, from the decomposition the set of *m* matrices with the size *(i, j)* is obtained. Then the EEMD is applied in the second - vertical - direction, on the columns. It means that all columns from every *RX*-matrix are decomposed into *n* components. Again the corresponding components are collected into the matrix marked *CRX*. From each *RX*-matrix, number of *n CRX*-matrices with the size *(i, j)* is obtained, which means that the decomposition of *X(i, j)* leads to the set of $m \times n$ matrices. Those matrices represent the 2D EEMD components, they can be rewritten to one matrix *CRX(m, n)*:

$$CRX(m,n) = \begin{pmatrix} crx_{1,1} & crx_{2,1} & \cdots & crx_{m,1} \\ crx_{1,2} & crx_{2,1} & \cdots & crx_{m,2} \\ \vdots & \vdots & \vdots & \vdots \\ crx_{1,n} & crx_{2,n} & \cdots & crx_{m,n} \end{pmatrix} \tag{3.8}$$

To obtain the 2D features these components have to be combined somehow. In [10] the comparable minimal scale combination principle is described. The principle is that the components of the same or comparable scales with minimal difference are combined. In the (3.8) the components of the first row and first column are considered to be approximately the same, thus the first 2D component ($C2D_1$) is formed by their combination. The other 2D components have to be created by the same combination technique, generally:

$$C2D_l = \sum_{m=l}^{m} crx_{m,l} + \sum_{n=l+1}^{n} crx_{l.n}, \tag{3.9}$$

where *l* is the index of C2D and it is determined as:

$$\begin{array}{ll} l = m = n & if\ m = n \\ l = m & if\ m < n. \\ l = n & if\ m > n \end{array} \tag{3.10}$$

Considering, that this work deals with 2D data, the equation for multi-dimensional data decomposition will not be mentioned.

In the paper [10] the MDEEMD was used for the filtration of two-dimensional nonlinear geophysical data. The proposed method applies piecewise cubic Hermite interpolating polynomial (PCHIP) for the interpolation of the extrema envelopes which should interpolate the lower frequency components better, compared to the cubic polynomial spline. At first the proposed method was applied to an artificially noised image, which was then decomposed and reconstructed with the contribution of only some components. This process was performed twice with different interpolation methods - PCHIP method and the cubic spline interpolation. The results were then compared. As an example of real data processing the set of 2D magnetic data was used, with the number of 6 IMFs for each decomposition being determined at the beginning.

The paper [36] describes a variation of EEMD method - complete ensemble empirical mode decomposition with adaptive noise (CEEMDAN). This method should be able to provide the reconstruction of the original data with less error and lower number of sifting iterations. There is a description of CEEMDAN for one-dimensional signal *x[n]*. First the *I* realizations of *x[n]* with different white Gaussian noise are computed:

$$x[n] + \varepsilon_0 w^i[n], \tag{3.11}$$

where w^i being the i^{th} realization of white noise and ε_0 marks the noise standard deviation. Each $x^i[n]$ is decomposed by EMD. Then the first ensemble component is computed:

$$\widetilde{IMF_1}[n] = \frac{1}{I}\sum_{i=1}^{I} IMF_1^i[n] = \overline{IMF_1}[n], \tag{3.12}$$

and the first residue $r_1[n]$ is obtained by subtraction of the $\widetilde{IMF_1}[n]$ from the *x[n]*.

This residue is then noised with *I* different realizations of white noise, w^i, and decomposed to the first modes. The average value of these *I* modes gives the second component - $\widetilde{IMF_2}$. This approach can be described by defining new operator $E_j(\cdot)$. $E_j(\cdot)$ is designed to produce j^{th} mode with the EMD. For *k* = 2, ..., *K* the k^{th} residue is defined as:

$$r_k[n] = r_{k-1}[n] - \widetilde{IMF_k}[n], \tag{3.13}$$

from which the $(k+1)^{th}$ IMF is computed as:

$$\widetilde{IMF_{k+1}}[n] = \frac{1}{I}\sum_{i=1}^{I} E_1(r_k[n] + \varepsilon_k E_k(w^i[n])). \tag{3.14}$$

The original signal can be then written as:

$$x[n] = \sum_{k=1}^{K} \widetilde{IMF_k} + R[n], \tag{3.15}$$

where *R[n]* marks the final residue, which cannot be decomposed. [36]

An improved CEEMDAN method with the extension for multi-dimensional data was applied to Laser Speckle Contrast Images in the paper [21]. The multi-dimensional extension algorithm was the same as the one described in [10], using the comparable minimal scale.

3.4 Eigenvalue decomposition

The eigenvalue decomposition (EVD) provides the eigenvectors and eigenvalues of input data $\boldsymbol{x}$. Eigenvalues and eigenvectors are computed from the covariance matrix of data $\boldsymbol{x}$. Sample covariance matrix $\widehat{\boldsymbol{R}}_{xx}$ is defined as:

$$\widehat{\boldsymbol{R}}_{\boldsymbol{xx}} = E\{\boldsymbol{x}\boldsymbol{x}^T\} = \boldsymbol{V}\Lambda\boldsymbol{V}^T \tag{3.16}$$

with $\boldsymbol{\Lambda}$ being a diagonal matrix containing eigenvalues $[\lambda_1, \lambda_2, ..., \lambda_m]$; $\boldsymbol{V} = [\boldsymbol{v}_1, \boldsymbol{v}_2, ..., \boldsymbol{v}_m]$ is corresponding orthogonal matrix with $\boldsymbol{v}_i$ being unit length eigenvectors - principal components. The problem to solve is formulated as:

$$\boldsymbol{R}_{xx}\boldsymbol{v}_i = \lambda_i\boldsymbol{v}_i, \tag{3.17}$$

where $\boldsymbol{R}_{xx} = E\{\boldsymbol{x}\boldsymbol{x}^T\}$, E is the expectation operator and $\boldsymbol{x}$ represents zero-mean signal. Usually covariance matrix $\boldsymbol{R}_{xx}$ is computed first and then some numerical method is applied to obtain its eigenvalues and eigenvectors. [8]

3.5 Singular value decomposition

Singular value decomposition (SVD) is also a technique able to compute eigenvectors. Unlike the EVD, the SVD does not use the covariance matrix but data itself. [18] The mixture $\boldsymbol{x}$ with dimensions *(m, N)* is in the SVD described as:

$$\boldsymbol{x} = \boldsymbol{U}\boldsymbol{\Sigma}\boldsymbol{V}^T. \tag{3.18}$$

$\boldsymbol{U}(m, m)$ and $\boldsymbol{V}(N, N)$ both represent orthogonal matrices of eigenvectors. $\boldsymbol{\Sigma}$ is an $m \times N$ pseudodiagonal matrix with first n rows containing singular values $\boldsymbol{\Sigma}_S = diag\{\sigma_1, \sigma_2, ..., \sigma_n\}$ and the remaining rows being zero. Columns of $\boldsymbol{V}$, also called the right singular vectors, are eigenvectors of the column-column correlation matrix $\boldsymbol{X}^T\boldsymbol{X}$. Similarly, columns of $\boldsymbol{U}$ are known as left singular vectors and they represent eigenvectors of the row-row correlation matrix $\boldsymbol{X}\boldsymbol{X}^T$. Singular values are then defined as the square roots of the eigenvalues in $\boldsymbol{X}^T\boldsymbol{X}$ or $\boldsymbol{X}\boldsymbol{X}^T$. From these, following equations are derived:

$$\boldsymbol{X}\boldsymbol{X}^T = \boldsymbol{U}\boldsymbol{\Sigma}_1^2\boldsymbol{U}^T, \tag{3.19}$$

$$\boldsymbol{X}^T\boldsymbol{X} = \boldsymbol{V}\boldsymbol{\Sigma}_2^2\boldsymbol{V}^T. \tag{3.20}$$

Variables $\boldsymbol{\Sigma}_1$ and $\boldsymbol{\Sigma}_2$ are defined as: $\boldsymbol{\Sigma}_1 = \text{diag}\{\sigma_1, ..., \sigma_m\}$, $\boldsymbol{\Sigma}_2 = \text{diag}\{\sigma_1, ..., \sigma_N\}$. [8] [30]

In the paper [30] an image denoising procedure using SVD is described. Noisy image A with noise $N(0, \sigma)$ serves as an input. First the individual image patches of size $p \times p$ are decomposed using the sliding window:

$$A_i = U_i\Sigma_i V_i^T, \tag{3.21}$$

where Σ_i represents the matrix of singular values. Then obtained singular values σ_i are processed. Paper [30] proposes three approaches. The first one is to calculate either rank 1 or rank 2 for each patch; the second one is to cancel out patch singular values smaller than defined threshold. The threshold used in this method was $\sigma\sqrt{2\log p^2}$.The last approach is to truncate patch singular values to get residual with standard deviation of σ. Finally, the filtered image is obtained by computing the average of overlapping pixels from patches. The paper [30] mainly brings another approach for image denoising - the Higher Order Singular Value Decomposition.

3.6 Independent component analysis

The independent component analysis (ICA) is based on the idea of the separation of the original signals from their noised mixture. As an introduction to the problematics the *cocktail-party problem* is often used. Two microphones placed in different positions in the room record sounds of two people speaking at the same time. Recorded signals $x_1(t)$ and $x_2(t)$, obtained from microphones, can be expressed as:

$$\begin{aligned} x_1(t) &= a_{11}s_1 + a_{12}s_2 \\ x_2(t) &= a_{21}s_1 + a_{22}s_2, \end{aligned} \tag{3.22}$$

where a_{11}, a_{12}, a_{21}, a_{22} are parameters determined by the distance between the microphones and speaking people and $s_1(t)$, $s_2(t)$ are the two original speech signals. The task is to separate $s_1(t)$ and $s_2(t)$ from the recorded signals $x_1(t)$ and $x_2(t)$ without any information about the parameters a_{ii}. The ICA is based on the assumption of the signals $s_1(t)$ and $s_2(t)$ being independent.

When observing linear mixtures of n independent components (ICs), the j^{th} observation x_j can be described as:

$$x_j = a_{j1}s_1 + a_{j2}s_2 + \cdots + a_{jn}s_n. \tag{3.23}$$

In the vector-matrix notation it is transcribed as

$$\mathbf{x} = \mathbf{A}\mathbf{s}, \tag{3.24}$$

where **x** and **s** are column vectors and **A** is matrix. As mentioned above, only **x** is observed, thus, **A** and **s** are unknown and have to be estimated. The basic ICA model assumes, besides the statistical independency of the independent components, that their distributions are unknown. When the matrix **A** is estimated, its inverse matrix **W** is determined. Then the independent components **s** are computed as: [22]

$$\mathbf{s} = \mathbf{W}\mathbf{x}. \tag{3.25}$$

The independency of two sources can be expressed by the joint probability density function (pdf) $p_{1,2}(s_1, s_2)$:

$$p_{1,2}(s_1, s_2) = p_1(s_1)p_2(s_2), \tag{3.26}$$

with $p_1(s_1)$ and $p_2(s_2)$ being the marginal pdfs. The basic pre-processing of the input data is usually centering the data, which means the subtraction of the mean value, and the data whitening. [6]

Whitening is an operation when the observed data vector **x** is linearly multiplied by matrix $\boldsymbol{V_w}$:

$$\boldsymbol{z} = \boldsymbol{V_w}\boldsymbol{x}, \tag{3.27}$$

where **z** marks the whitened data. White vector contains uncorrelated components with unit variances. One approach in whitening is the EVD of the covariance matrix $E\{\boldsymbol{x}\boldsymbol{x}^T\}$, which is described in equation (3.16). Then the whitening matrix is defined as:

$$\boldsymbol{V_w} = \boldsymbol{V}\Lambda^{-1/2}\boldsymbol{V}^T. \tag{3.28}$$

The whitening process eases the searching for the mixing matrix, which is reduced for searching in the space of orthogonal matrices. [23]

3.6.1 Maximization of Nongaussianity

In this approach the nongaussianity is used to estimate the independent components. Nongaussianity has to be quantitative measured first, which is realized via computing the kurtosis. Kurtosis is defined as the fourth-order cumulant of a random variable; for random variable *y* the kurtosis *kurt(y)* is computed as:

$$kurt(y) = E\{y^4\} - 3(E\{y^2\})^2. \tag{3.29}$$

It is assumed that *y* is normalized with variance $E\{y^2\} = 1$, which means that the right side of the equation simplifies to $E\{y^4\} - 3$. Kurtosis can be either negative (subgaussian random variable) or positive (supergaussian random variable); for gaussian variable the value is zero. Supergaussian variable typically have Laplacian distribution. Nongaussianity is usually expressed as the absolute value of kurtosis.

Maximizing process starts with some vector $\boldsymbol{w}$. The absolute value of kurtosis of $y = \boldsymbol{w}^T\boldsymbol{z}$ is computed and then the direction of its strongest growth is determined. Vector $\boldsymbol{w}$ is then moved in that direction. An adaptive gradient algorithm is described as:

$$\Delta\boldsymbol{w} \propto sign\big(kurt(\boldsymbol{w}^T\boldsymbol{z})\big)\boldsymbol{z}(\boldsymbol{w}^T\boldsymbol{z})^3 \tag{3.30}$$

$$\boldsymbol{w} \leftarrow \boldsymbol{w}/\|\boldsymbol{w}\|. \tag{3.31}$$

Every observation ***z(t)*** is used only once and the time-average estimation of the kurtosis, γ, is computed from the equation: [23]

$$\Delta\gamma \propto ((\boldsymbol{w}^T\boldsymbol{z})^4 - 3) - \gamma. \tag{3.32}$$

Nongaussianity by negengropy

The negentropy is another way to measure the nongaussianity of the data. The entropy is the property of data connected with the contained information. Unpredictable and unstructured data have larger entropy than data which are less "random". The entropy *H* of a random vector $\boldsymbol{y}$ is defined as:

$$H(y) = -\int p_y(\boldsymbol{\eta}) log\, p_y(\boldsymbol{\eta}) d\boldsymbol{\eta}, \tag{3.33}$$

where $p_y(\boldsymbol{\eta})$ is the density of $\boldsymbol{y}$. Entropy is the largest for variables which are gausssian, thus it can be used for the measurement of nongaussianity. For this purpose, the negentropy *J* is defined:

$$J(\boldsymbol{y}) = H\big(\boldsymbol{y}_{gauss}\big) - H(\boldsymbol{y}). \tag{3.34}$$

The variable $\boldsymbol{y}_{gauss}$ marks random variable of the same correlation and covariance matrix as $\boldsymbol{y}$. [23]

In the [23] two FastICA algorithms using negentropy are proposed. One employs deflationary orthogonalization and the other employs symmetric orthogonalization. The steps of the first algorithm are described below. First the data is centered and whitened, to obtain the input $\boldsymbol{z}$. Then m, the required number of ICs is chosen, and an initial random $\boldsymbol{w}_p$ with unit norm is defined. The index p has initial value equal 1 and increases from 1 to m. The $\boldsymbol{w}_p$ is recalculated as:

$$\boldsymbol{w}_p \leftarrow E\left\{\boldsymbol{z}g(\boldsymbol{w}_p^T\boldsymbol{z})\right\} - E\left\{g'(\boldsymbol{w}_p^T\boldsymbol{z})\right\}\boldsymbol{w}. \tag{3.35}$$

The function g can be defined e.g. as one of these:

$$g_1(y) = \tanh(a_1 y) \tag{3.36}$$

$$g_2(y) = y\exp\left(\frac{-y^2}{2}\right) \tag{3.37}$$

$$g_3(y) = y^3. \tag{3.38}$$

Constant a_1 takes value from the interval <1, 2>. Next step is to orthogonalize $\boldsymbol{w}_p$:

$$\boldsymbol{w}_p \leftarrow \boldsymbol{w}_p - \sum_{j=1}^{p-1}(\boldsymbol{w}_p^T\boldsymbol{w}_j)\boldsymbol{w}_j, \tag{3.39}$$

and finally

$$\boldsymbol{w}_p \leftarrow \boldsymbol{w}_p/\|\boldsymbol{w}_p\|. \tag{3.40}$$

If $\boldsymbol{w}_p$ has not converged, the process returns to the equation (3.35) and continues from there. The value of p is increased by 1, and if it fits the condition $p \leq m$, a new initial random $\boldsymbol{w}_p$ is defined to obtain another IC.

The second algorithm, as mentioned above, uses symmetric orthogonalization. The input data is preprocessed the same way as in the previous algorithm. Then required number of ICs, m, is chosen. When having the number, m initial vectors $\boldsymbol{w}_i$, $i = 1, ..., m$ are defined, each one of unit norm. Matrix $\boldsymbol{W}$, $\boldsymbol{W} = (\boldsymbol{w}_1, ..., \boldsymbol{w}_m)^T$ is orthogonalized:

$$\boldsymbol{W} \leftarrow (\boldsymbol{W}\boldsymbol{W}^T)^{-1/2}\boldsymbol{W}. \tag{3.41}$$

Then each $\boldsymbol{w}_i$ is recomputed as:

$$\boldsymbol{w}_i \leftarrow E\{\boldsymbol{z}g(\boldsymbol{w}_i^T\boldsymbol{z})\} - E\{g'(\boldsymbol{w}_i^T\boldsymbol{z})\}\boldsymbol{w}, \tag{3.42}$$

with g being one of the functions (3.36), (3.37), (3.38). Then the matrix $\boldsymbol{W}$ is orthogonalized again, according to the equation (3.41). If it has not converged, the process returns to the step where each $\boldsymbol{w}_i$ is recomputed (equation 3.42) and continues from there. [23]

3.6.2 Maximum likelihood estimation

This method is based on the using of the density p_x of the mixture vector $\boldsymbol{x}$. The density is given as:

$$p_x(\boldsymbol{x}) = |\det \boldsymbol{B}| p_s(s) = |\det \boldsymbol{B}| \prod_i p_i(s_i), \tag{3.43}$$

with $\boldsymbol{B}$ being defined as $\boldsymbol{B} = \boldsymbol{A}^{-1}$ and p_i is the density of independent component.

The FastICA algorithm employing this estimation consists of several steps. First the data are centered and the correlation matrix $\boldsymbol{R}_{xx}$ is computed as:

$$\boldsymbol{R}_{\boldsymbol{xx}} = E\{\boldsymbol{x}\boldsymbol{x}^T\}. \tag{3.44}$$

An initial random separating matrix $\boldsymbol{B}$ is defined. Then the $\boldsymbol{y}$ is obtained as the product of $\boldsymbol{B}$ and $\boldsymbol{x}$. Then the values β_i and α_i are computed:

$$\beta_i = -E\{y_i g(y_i)\}, \tag{3.45}$$

$$\alpha_i = -\frac{1}{\beta_i + E\{g'(y_i)\}}, \tag{3.46}$$

both for $i = 1, ..., n$ with g usually marking the tanh function. Then the separation matrix $\boldsymbol{B}$ is recomputed:

$$\boldsymbol{B} \leftarrow \boldsymbol{B} + diag(\alpha_i)[diag(\beta_i) + E\{\boldsymbol{g}(\boldsymbol{y})\boldsymbol{y}^T\}]\boldsymbol{B}. \tag{3.47}$$

Matrix B is then decorrelated and normalized:

$$\boldsymbol{B} \leftarrow (\boldsymbol{B}\boldsymbol{R}_{\boldsymbol{xx}}\boldsymbol{B}^T)^{-1/2}\boldsymbol{B}. \tag{3.48}$$

If the result does not converge, the process returns to the computation of the $\boldsymbol{y}$ and from there it is repeated. [23]

3.6.3 Minimization of mutual information

By the term mutual information, a measure of the dependence between random variables is meant. This value equals zero just in one special case - when the variables are statistically independent. Estimated components $\boldsymbol{s}$ are described by this invertible transformation:

$$\boldsymbol{s} = \boldsymbol{B}\boldsymbol{x}, \tag{3.49}$$

where the matrix $\boldsymbol{B}$ has such properties that the mutual information of components s_i is minimized. Mutual information I between n scalar random variables $y_i, .., y_n$ can be obtained from the equation:

$$I(y_1, y_2, \dots, y_n) = -\sum_i E\{G_i(y_i)\} - \log|\det B| - H(x), \tag{3.50}$$

where $G_i(y_i) = log\ p_i(y_i)$, with p_i being the probability density function. The estimating algorithm is similar to the ones mentioned in the section 3.6.1. [23]

3.6.4 Spatial independent component analysis

The result of spatial ICA (sICA) is a set of mutually independent images. Each column of the input mixing matrix $\boldsymbol{x}$ represents one image, transformed to the vector by the concatenation of its rows. This vectorization does not affect the results because ICA works only with the gray levels of pixels, not with their order. Thus, sICA assumes that the spatial pattern is independent over space. [32]

In the paper [22] an image denoising using ICA is described. Individual observations of just one image were obtained as sample windows (patches) from random image locations. Each sample window was vectorized.

3.6.5 Image denoising with Independent component analysis

The paper [6] describes four ICA methods applied to reduce the speckle noise in retinal optical coherence tomography (OCT) images. The proposed methods are InfoMax, Second Order Blind Identification (SOBI), FastICA and Joint Approximate Diagonalization of Eigen-matrices (JADE). Two approaches for FastICA are described in the 3.6.1, for the other methods their basic descriptions are below. In [6] the filtered B-scan images were firstly vectorized and formed to a matrix. Then individual ICA methods were applied, and from the obtained independent components the main component was considered to be the noise-free image.

InfoMax

The first proposed method is InfoMax. This method is based on the maximization of the mutual information and it is realized using the neural network. The mutual information I is described as:

$$I(Y, X) = H(Y) - H(Y|X), \tag{3.51}$$

where Y represents the network's output and X is input. $H(Y)$ is then entropy of Y and $H(Y|X)$ is entropy of Y which is not a result of X. Variable w represents the network's parameter, independent on $H(Y|X)$ and related to the gradients of $I(Y, X)$ and $H(Y)$. On the basis of this, following equation can be written:

$$\frac{\partial}{\partial w} I(X, Y) = \frac{\partial}{\partial w} H(Y). \tag{3.52}$$

The output vector $\boldsymbol{y}$ from the neural network is then:

$$\boldsymbol{y} = g(\boldsymbol{W}\boldsymbol{x}) + \boldsymbol{w}_0, \tag{3.53}$$

where $\boldsymbol{x}$ is network's input vector, $\boldsymbol{W}$ is weight matrix, $\boldsymbol{w}_0$ is bias vector and g substitutes a sigmoidal function; $g(u) = (1+e^{-u})^{-1}$. With $\boldsymbol{1}$ being a vector of ones, the iteration process for $\boldsymbol{W}$ is:

$$\Delta\boldsymbol{W} \propto [\boldsymbol{W}^T]^{-1} + (\boldsymbol{1} - 2\boldsymbol{y})\boldsymbol{x}^T. \tag{3.54}$$

The iteration process is repeated until $\boldsymbol{W}$ reaches convergence. [6]

SOBI

The Second Order Blind Identification (SOBI) method employs the idea of the source signals being affected by noise. In this case the observation $\boldsymbol{x}$ is expressed as:

$$\boldsymbol{x} = \boldsymbol{A}\boldsymbol{s} + N, \tag{3.55}$$

where **A** is full-ranked complex matrix and N marks the noise, which is assumed to be white and uncorrelated with source signals. SOBI algorithm has several steps. First the observed signals $\boldsymbol{x}$ are orthogonalized with the orthogonalization matrix $\boldsymbol{Q}$:

$$\bar{x} = \boldsymbol{Q}x, \tag{3.56}$$

then the set of covariance matrices is estimated:

$$\widehat{\boldsymbol{R}}_{\bar{x}}(p_i) = \frac{1}{N}\sum_{k=1}^{N} \bar{x}(k)\bar{x}^T(k - p_i) = \boldsymbol{Q}\widehat{\boldsymbol{R}}_x(p_i)\boldsymbol{Q}^T. \tag{3.57}$$

In the equation (3.57) N is the number of samples, p_i represents the time lag. Next step is to estimate the orthogonal matrix $\boldsymbol{U}$ and diagonal matrices $\boldsymbol{D}_i$ to perform the Joint Approximate Diagonalization (JAD):

$$\boldsymbol{R}_{\bar{x}}(p_i) = \boldsymbol{U}\boldsymbol{D}_i\boldsymbol{U}^T. \tag{3.58}$$

$\boldsymbol{U}$ can be estimated using some numerical algorithm, in [8] the Alternating Least Square technique is mentioned. When having the estimation of $\boldsymbol{U}$, source signals are estimated as:

$$\hat{s} = \boldsymbol{U}^T\boldsymbol{Q}\boldsymbol{x} \tag{3.59}$$

and the mixing matrix $\widehat{W}$ is: [6] [8]

$$\widehat{\boldsymbol{W}} = \boldsymbol{Q}^+\boldsymbol{U}. \tag{3.60}$$

JADE

The last proposed algorithm, JADE, is related to the SOBI. Data are either prewhitened or orthogonalized first. Preprocessed vector is marked $\bar{\boldsymbol{x}}$. Then sampled contracted quadricovariance matrix is decomposed with EVD:

$$\boldsymbol{C}_{\bar{\boldsymbol{x}}}(\boldsymbol{I}) = \frac{1}{N}\sum_{k=1}^{N}[\bar{\boldsymbol{x}}^T(k)\bar{\boldsymbol{x}}(k)\bar{\boldsymbol{x}}(k)\bar{\boldsymbol{x}}^T(k)]\} - 2\widehat{\boldsymbol{R}}_{\bar{\boldsymbol{x}}}(0)\widehat{\boldsymbol{R}}_{\bar{\boldsymbol{x}}}(0) - tr\left(\widehat{\boldsymbol{R}}_{\bar{\boldsymbol{x}}}(0)\right)\widehat{\boldsymbol{R}}_{\bar{\boldsymbol{x}}}(0) = \widehat{\boldsymbol{U}}\Lambda_{\boldsymbol{I}}\widehat{\boldsymbol{U}}^T. \tag{3.61}$$

In the equation (3.61) variable $\widehat{\boldsymbol{R}}_{\bar{\boldsymbol{x}}}(0)$ is defined as:

$$\widehat{\boldsymbol{R}}_{\bar{\boldsymbol{x}}}(0) = \frac{1}{N}\sum_{k=1}^{N}[\bar{\boldsymbol{x}}(k)\bar{\boldsymbol{x}}^T(k)]\} \tag{3.62}$$

and $\widehat{\boldsymbol{U}} = [\widehat{\boldsymbol{u}}_1, \widehat{\boldsymbol{u}}_2, \ldots, \widehat{\boldsymbol{u}}_n]$. Next step is to estimate *n* sampled quadricovariance matrices:

$$\boldsymbol{C}_{\bar{\boldsymbol{x}}}(\boldsymbol{E}_{\boldsymbol{p}}) = \frac{1}{N}\sum_{k=1}^{N}\left[\bar{\boldsymbol{x}}^T(k)\boldsymbol{E}_{\boldsymbol{p}}\bar{\boldsymbol{x}}(k)\bar{\boldsymbol{x}}(k)\bar{\boldsymbol{x}}^T(k)\right]\} - 2\widehat{\boldsymbol{R}}_{\bar{\boldsymbol{x}}}(0)\boldsymbol{E}_{\boldsymbol{p}}\,\widehat{\boldsymbol{R}}_{\bar{\boldsymbol{x}}}(0) - tr\left(\widehat{\boldsymbol{E}_{\boldsymbol{p}}\boldsymbol{R}_{\bar{\boldsymbol{x}}}}(0)\right)\widehat{\boldsymbol{R}}_{\bar{\boldsymbol{x}}}(0) - \widehat{\boldsymbol{R}}_{\bar{\boldsymbol{x}}}\boldsymbol{E}_p^T\,\widehat{\boldsymbol{R}}_{\bar{\boldsymbol{x}}}\,, \tag{3.63}$$

with $\boldsymbol{E}_p = \hat{\boldsymbol{u}}_p\hat{\boldsymbol{u}}_p{}^T$, for *p = 1, 2, ..., n*. Then for all *n* matrices $\boldsymbol{C}_{\bar{\boldsymbol{x}}}(\boldsymbol{E}_{\boldsymbol{p}})$ an orthogonal joint diagonalization matrix $\boldsymbol{U}$ is found, using some numerical method. Finally, the mixing matrix is defined as: [6] [8]

$$\widehat{W} = \boldsymbol{Q}^{+}\widehat{\boldsymbol{A}} = \boldsymbol{Q}^{+}\boldsymbol{U}. \tag{3.64}$$

3.7 Principal component analysis

Principal component analysis (PCA) is a technique widely used for feature extraction, data compression and statistical analysis. [8] This method, unlike the ICA, is able to distinguish source signals which are gaussian and uncorrelated. Sources are separated on the basis of their variance, where the sources with high variance are considered to be more important than the others. The obtained source signals are independent just in case that they are gaussian. Transformation between the observed signal mixture $\boldsymbol{x} = (x_1, x_2)^T$ and the extracted source signals $\boldsymbol{s} = (s_1, s_2)^T$ is described by matrix $\boldsymbol{W}_{pca}$:

$$\boldsymbol{s} = \boldsymbol{W}_{pca}\boldsymbol{x}, \tag{3.65}$$

with each row of $\boldsymbol{W}_{pca}$ representing one eigenvector. Thus, $\boldsymbol{W}_{pca}$ is presented as:

$$\boldsymbol{W}_{pca} = (\boldsymbol{w}_1, \boldsymbol{w}_2)^T. \tag{3.66}$$

Each $\boldsymbol{w}_i$ has unit length and it is able to distinguish only one source signal (principal component, PC) $\boldsymbol{s}_i$. An eigenvalue λ is the variance of individual PC. A task for PCA is to find such eigenvectors that the product of individual eigenvector $\boldsymbol{w}_i$ and signal mixture $\boldsymbol{x}$ produces individual signal s_i with variance $\sigma_i{}^T$:

$$s_i = \boldsymbol{w}_i^T \boldsymbol{x}. \tag{3.67}$$

The variance of extracted signals decreases from the first one (maximal variance) to the last one extracted. This is used for the data size reduction. [32]

PCA is closely related to the SVD and EVD algorithms. SVD can be applied to the covariance matrix instead of PCA or EVD, however its problem is that for large matrices X the algorithms can become computationally costly. EVD is also presented as one of the approaches for obtaining the eigenvalues and eigenvectors for PCA. [8]

3.7.1 Principal component analysis of an image

PCA is widely used for pattern recognition and dimension reduction. It can also serve as denoising tool - only most significant principal components of noised image are used to form the filtered image, while the rest of components containing the noise and trivial information is removed. [44]

The paper [44] proposes an improved PCA algorithm - Two-stage image denoising by principal component analysis with local pixel grouping. The basic scheme consists of two stages, which differ only in the parameter of noise level. In the first stage the input is the noisy image. Local pixel grouping is applied and then PCA transform and denoising is done. Finally, inverse PCA transformation is applied. The output of this stage serves as input for the second stage, where all the steps named above are undertaken. The final output is denoised image. In this method the noise is assumed to be white.

Another approach is described in [27] - MRI noise estimation and denoising using non-local PCA. PCA algorithm is employed only in the first stage of the process, while in the second stage the filtered image serves as a guide image for another filtering. Noised image is divided into 3D patches using sliding 3D window; for each 3D patch a group of the most similar patches is found. Every patch group is then decomposed using PCA and then the components with a standard deviation lower than defined threshold τ are eliminated. The last step is to combine all the estimations of each voxel with some uniform averaging rule. In the second stage the pre-filtered image was used as the guide image for non-local means filtering. Further description of proposed methods is in [27].

3.8 Filtered image quality assessment

The performance of the filtration has to be objectively evaluated. In the following paragraphs some basic metrics and image quality assessment (IQA) techniques will be described.

The two basic metrics for image noise measurement are the contrast-to-noise ratio (CNR) and the signal-to-noise ratio (SNR). CNR is given by:

$$CNR = \frac{|\mu_1 - \mu_2|}{\sqrt{\sigma_1^2 + \sigma_2^2}}, \tag{3.68}$$

where μ_1 and μ_2 are the expectation values and σ_1 and σ_2 stand for standard deviations of two image zones with different brightness. CNR is applicable only if there are at least two distinguishable areas. SNR is defined as:

$$SNR = \frac{\mu}{\sigma}, \tag{3.69}$$

with μ being the signal value and σ being the standard deviation, both related to the signal peak in the analyzed image. [35]

Paper [38] divides image quality metrics into three classes. The first class comprises methods that are called full-reference. Those metrics assumes the availability of the original image free from the distortion. The second class includes methods based on the partial knowledge about the original (reference) image - reduced-reference assessment. It can be in a form of some features. Finally, methods from the third class work with the assumption that no reference image is available, thus the image quality assessment is "blind" - called no-reference assessment.

3.8.1 Full-reference assessment methods

Widely used metric is the mean square error (MSE) and the peak signal to noise ratio (PSNR), based on MSE. The MSE value is obtained from the equation:

$$MSE = \frac{1}{M \times N} \sum_{i=1}^{M} \sum_{j=1}^{N} [x(i,j) - y(i,j)]^2, \tag{3.70}$$

where *x(i, j)* is the pixel value in the original image, *y(i, j)* is the pixel value in the filtered image and *(M × N)* is the size of image. The PSNR is then calculated as:

$$PSNR = 10\, log_{10} \left[\frac{(2^d - 1)^2}{MSE} \right], \tag{3.71}$$

where *d* stands for the number of bits. MSE basically describes the similarity between the original and the filtered image. [9] [34]

Structural similarity index

The structural similarity index (SSIM) [38], defined as:

$$SSIM(\boldsymbol{x}, \boldsymbol{y}) = [l(\boldsymbol{x}, \boldsymbol{y})]^{\alpha} \cdot [c(\boldsymbol{x}, \boldsymbol{y})]^{\beta} \cdot [s(\boldsymbol{x}, \boldsymbol{y})]^{\gamma} \tag{3.72}$$

is based on the assumption that the human visual system (HVS) focuses mainly on the structural information contained in the image. In the equation (3.72) variables ***x***, ***y*** represent two image signals which are compared (i.e. the reference and the distorted image). SSIM employs three comparison functions - luminance, contrast and structure comparison function. The luminance comparison function *l(**x**, **y**)* is described as:

$$l(\boldsymbol{x}, \boldsymbol{y}) = \frac{2\mu_x\mu_y + C_1}{\mu_x^2 + \mu_y^2 + C_1}, \tag{3.73}$$

with μ_x and μ_y being the mean intensities and C_1 defined as:

$$C_1 = (K_1 L)^2. \tag{3.74}$$

where K_1 is small constant. L stands for the range of pixel values.

Contrast comparison function is given by:

$$c(\boldsymbol{x}, \boldsymbol{y}) = \frac{2\sigma_x\sigma_y + C_2}{\sigma_x^2 + \sigma_y^2 + C_2}, \tag{3.75}$$

with C_2 obtained as:

$$C_2 = (K_2 L)^2, \tag{3.76}$$

and K_2 being some small constant. The signal contrast is estimated as the standard deviation - variables σ_x and σ_y.

The last function to be defined is the structure comparison function *s(**x**, **y**)*:

$$s(\boldsymbol{x}, \boldsymbol{y}) = \frac{\sigma_{xy} + C_3}{\sigma_x\sigma_y + C_3}. \tag{3.77}$$

In this equation (3.77) C_3 is constant and σ_{xy} is estimated as:

$$\sigma_{xy} = \frac{1}{N-1}\sum_{i=1}^{N}(x_i - \mu_x)(y_i - \mu_y). \tag{3.78}$$

In the (3.72) these three functions *l(**x**, **y**)*, *c(**x**, **y**)* and *s(**x**, **y**)* have individual relative importance corrected by the parameters $\alpha > 0$, $\beta > 0$ and $\gamma > 0$. [38]

3.8.2 No-reference assessment methods

In the paper [28] two methods using some transform are mentioned. The first one, called the Distortion Identification-based Image INtegrity and Verity Evaluation (DIIVINE) works with statistical values obtained using wavelet coefficient model. The second method is the BLind Notator Using DCT Statistic (BLIINDS-II index). DCT stands for the discrete cosine transform which is used to obtain statistical features. Both methods are based on the natural scene statistics (NSS) models. However, the paper [28] mainly proposes the blind/referenceless image spatial quality evaluator (BRISQUE).

BRISQUE method differs in the fact that it does not employ any transform. First an input image *I* is operated as:

$$\hat{I}(i,j) = \frac{I(i,j) - \mu(i,j)}{\sigma(i,j) + C}, \tag{3.79}$$

where *(i, j)* are spatial coordinates of the image with size *(M × N)* and *C = 1* is constant. Values *Î(i, j)* are called mean subtracted contrast normalized (MSCN) coefficients. Local mean *μ(i, j)* is then defined as:

$$\mu(i,j) = \sum_{k=-K}^{K} \sum_{l=-L}^{L} w_{k,l} I_{k,l}(i,j), \tag{3.80}$$

and local variance *σ(i, j)* is defined as:

$$\sigma(i,j) = \sqrt{\sum_{k=-K}^{K} \sum_{l=-L}^{L} w_{k,l} \left(I_{k,l}(i,j) - \mu(i,j)\right)^2}. \tag{3.81}$$

In the equations (3.80) and (3.81) function *w* is a 2D circularly-symmetric Gaussian weighting function. Variables *K*, *L* represent the size of window. In [28] both *K* and *L* were equal 3.

Four differently oriented pairwise products of neighboring MSCN coefficients are defined - horizontal (H), vertical (V), main-diagonal (D1) and secondary-diagonal (D2) orientations:

$$H(i,j) = \hat{I}(i,j)\hat{I}(i,j+1) \tag{3.82}$$

$$V(i,j) = \hat{I}(i,j)\hat{I}(i+1,j) \tag{3.83}$$

$$D1(i,j) = \hat{I}(i,j)\hat{I}(i+1,j+1) \tag{3.84}$$

$$H(i,j) = \hat{I}(i,j)\hat{I}(i+1,j-1). \tag{3.85}$$

MSCN coefficients are used to form histograms. Histogram of a reference image free from distortion resembles the Gaussian distribution. Each distortion then changes the shape of histogram. As a model the asymmetric generalized Gaussian distribution (AGGD), marked *f*, is proposed:

$$f(x; v, \sigma_l^2, \sigma_r^2) = \begin{cases} \frac{v}{(\beta_l + \beta_r)\Gamma\left(\frac{1}{v}\right)} exp\left(-\left(-\frac{x}{\beta_l}\right)^v\right) & x < 0 \\ \frac{v}{(\beta_l + \beta_r)\Gamma\left(\frac{1}{v}\right)} exp\left(-\left(\frac{x}{\beta_l}\right)^v\right) & x \geq 0 \end{cases}, \tag{3.86}$$

where $\Gamma(\cdot)$ is gamma function, β_l is defined as:

$$\beta_l = \sigma_l \sqrt{\frac{\Gamma\left(\frac{1}{v}\right)}{\Gamma\left(\frac{3}{v}\right)}}, \tag{3.87}$$

and β_r is defined as:

$$\beta_r = \sigma_r \sqrt{\frac{\Gamma\left(\frac{1}{v}\right)}{\Gamma\left(\frac{3}{v}\right)}}. \tag{3.88}$$

Variable v is called the shape parameter, σ_l^2 and σ_r^2 are called scale parameters controlling the spread on both sides of the mode (r - right, l - left). In [28] those three parameters were estimated with the moment-matching based approach.

Different features can be obtained from the image by applying AGGD either on the MSCN coefficients or on individual pairwise products. Those features describe image distortions and assess image quality. In [28] obtained features were transformed from the feature space into quality scores using support vector machine regressor (SVR).

4. Practical part

The aim of this work was to filter TEM images without any information about the noise characteristic. All the applied methods are based on the decomposition of the image into certain specific components. Filtration in this work was based on the idea that proposed methods will decompose the input noisy image into a set of components. It was assumed that either one or more components will contain the noise and the rest will contain image information. It means that if the noisy image was decomposed in the ideal way, the filtered (noise-free) image could be obtained by the reverse composition of individual noise-free components while those, containing noise, are excluded from the composition.

Principal component analysis (PCA) was excluded from implementation because after a series of testing it came out that available methods assume, that images are corrupted with white noise. This does not correspond with the topic of this thesis.

Following chapter contains the description of used test data and applied filtration methods along with quality assessment methods. After series of testing these methods were chosen: bi-dimensional empirical mode decomposition (BEMD), ensemble empirical mode decomposition (EEMD), singular value decomposition (SVD) and independent component analysis (ICA). For all the Matlab functions, mentioned in the following paragraphs, further description can be found in [12].

4.1 Test data

All the images used as test data are real TEM images provided by the Thermo Fisher Scientifics. As a model data one HAADF HR STEM image was used; with size 512 x 512 px. It contains all the noises and distortions - high frequency noise, mechanical noise caused by vibrations and the influence of different thickness of the sample. It is in the Fig. 9.

One part of the testing set of images consists of 8 HAADF HR STEM images of Si, marked HAADF3 to HAADF10 (Fig. 10, Fig. 11, Fig. 12 and Fig. 13). Properties of individual images are summarized in the Table 1.

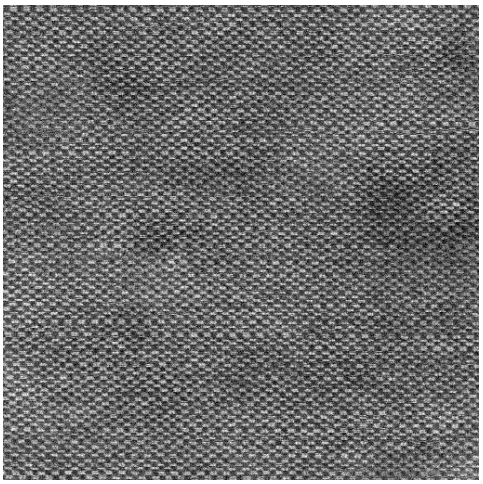

Fig. 9.: Model image

Table 1: HR STEM test images properties

name	size [px]	size [nm]	pixel size [pm]	magnification
HAADF3	512 x 512	21.00 x 21.00	41.00	5 100 000
HAADF4	512 x 512	14.90 x 14.90	29.00	7 200 000
HAADF5	512 x 512	14.90 x 14.90	29.00	7 200 000
HAADF6	512 x 512	7.43 x 7.43	14.50	14 500 000
HAADF7	512 x 512	7.43 x 7.43	14.50	14 500 000
HAADF8	512 x 512	21.00 x 21.00	41.00	5 100 000
HAADF9	512 x 512	21.00 x 21.00	41.00	5 100 000
HAADF10	512 x 512	21.00 x 21.00	41.00	5 100 000

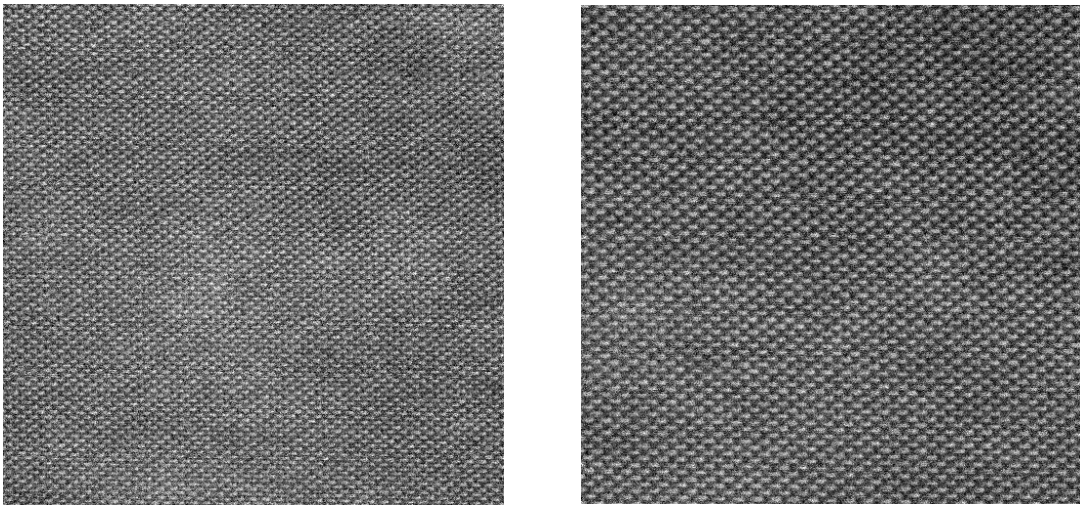

Fig. 10.: HR STEM images HAADF3 (left) and HAADF4 (right)

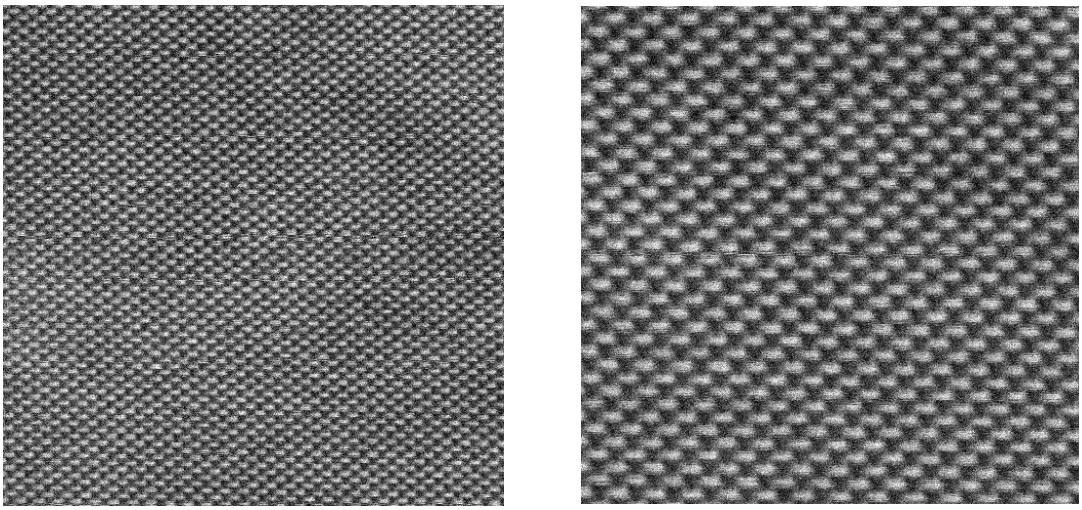

Fig. 11.: HR STEM images HAADF5 (left) and HAADF6 (right)

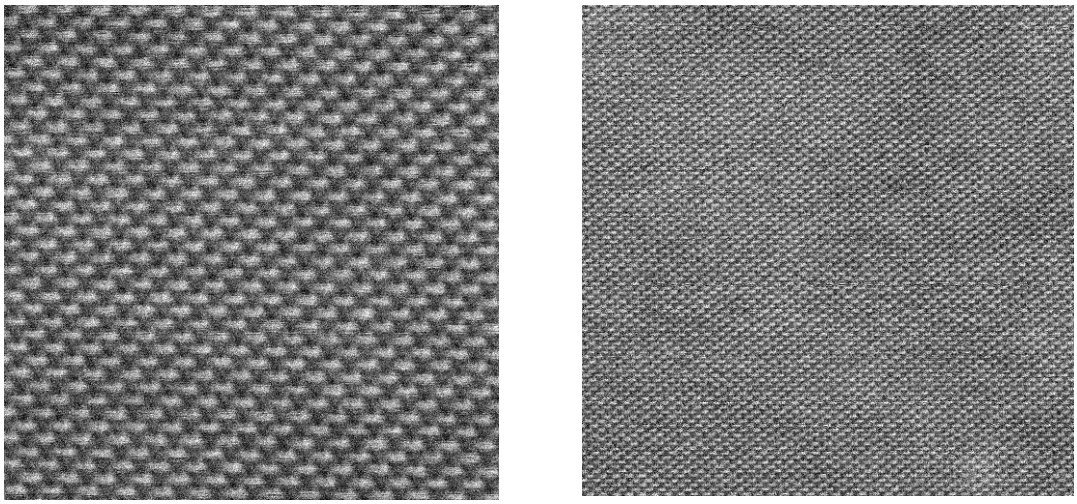

Fig. 12.: HR STEM images HAADF7 (left) and HAADF8 (right)

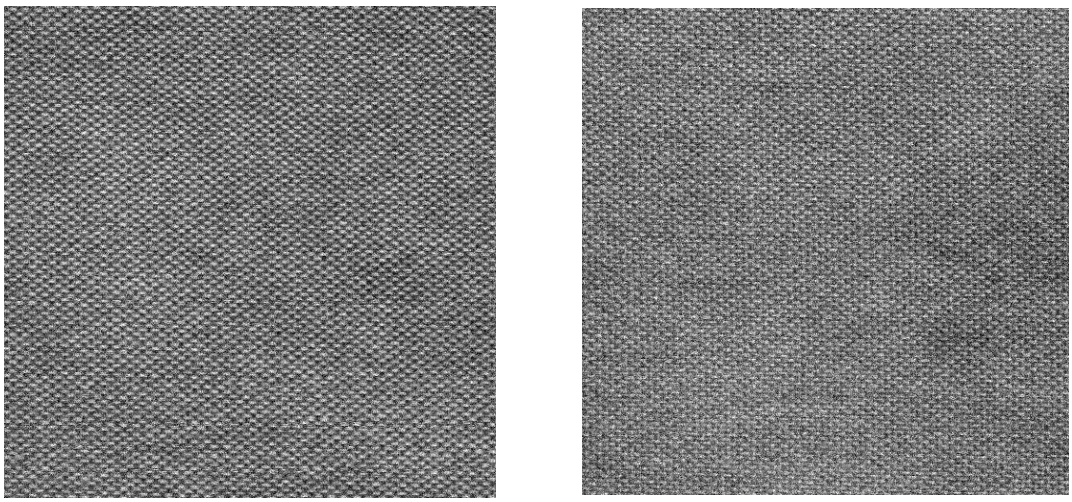

Fig. 13.: HR STEM images HAADF9 (left) and HAADF10 (right)

Along with STEM images of Si, 7 other images were tested; they are presented in Fig. 14, Fig. 15, Fig. 16 and Fig. 17. Images are named azbest3, carbon2, feritic6, gold_X, spinel2, Zn2 and ZnS14. Their properties are in Table 2.

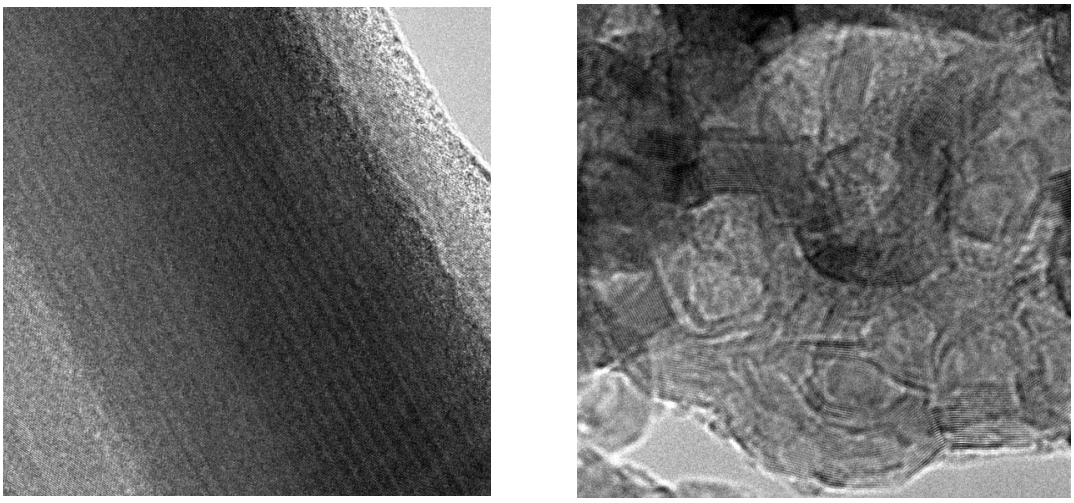

Fig. 14.: Images azbest3 (left), carbon2 (right)

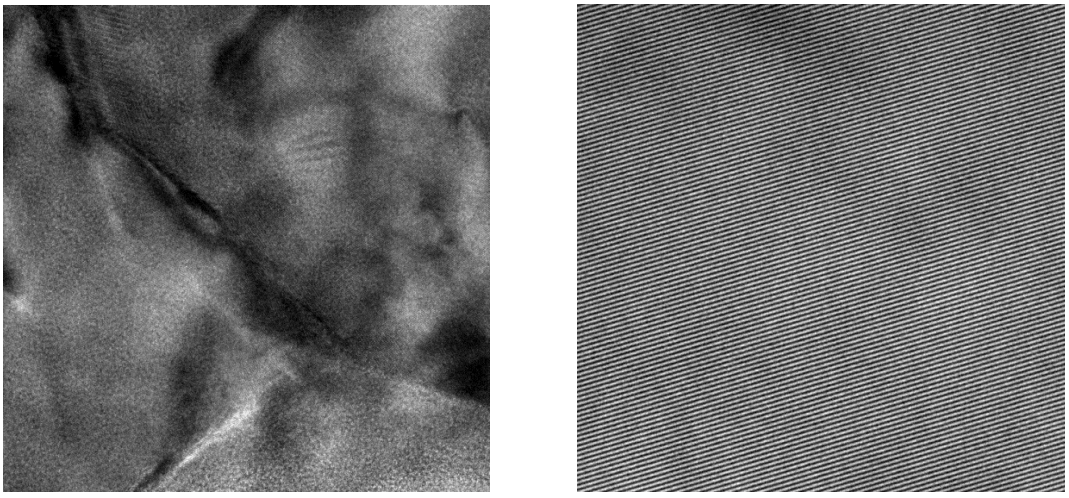

Fig. 15.: Images feritic6 (left), gold_X (right)

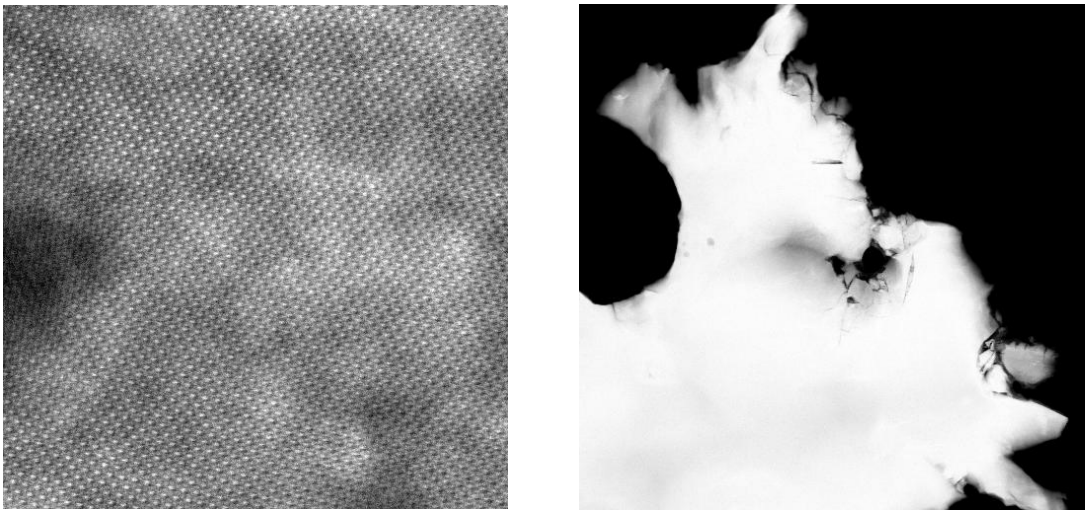

Fig. 16.: Images spinel2 (left), Zn2 (right)

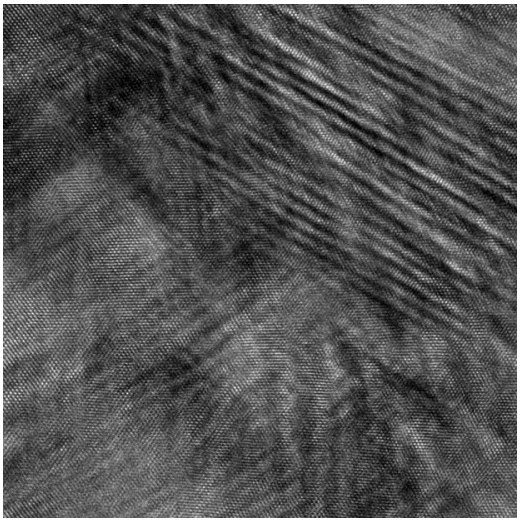

Fig. 17.: Image ZnS14

Table 2.: Properties of non-periodic texture images

name	size [px]
azbest3	1024 x 1024
carbon2	1024 x 1024
feritic6	1024 x 1024
gold_X	1024 x 1024
spinel2	512 x 512
Zn2	512 x 512
ZnS14	1024 x 1024

4.2 Applied image quality assessment methods

To assess the filtered images quality, four methods were applied. The first of them was MSE, which is computed according to the equation (3.70) in the paragraph 3.8.1. It basically describes mean pixel intensity difference between pixels in the input and filtered image on the same position. The lower this value is, the bigger is the difference between compared images. The second score was PSNR, computed via Matlab function `psnr`. The third used method was SSIM, also computed with Matlab function - `ssim`. This score also describes the similarity between input and filtered image, but with focus on the structure, luminance and contrast in compared images. Values close to 1 express that images are very similar; lower values mean less similarity. All three functions are computed via script `im_qual`.

These three scores are meant to be used when reference image is available - a noiseless image without distortion and blur. Then the filtered image is compared with this reference image to assess whether the filtration was successful. However, for this work no reference images were available, so these scores serve only to express whether there was some change at all.

The last applied method was the BRISQUE score. This score should assess the image quality without any reference. In this paper the function `brisquescore` was used. It was downloaded from [2]. In the description of the function it was said that usually the score is between 0 and 100, where 0 stands for the image of the highest quality and 100 for the opposite. There came up the first problem - for some images from the dataset the original score was higher than 100. Another problem appeared when filtered images were assessed - the score was sometimes even higher compared to the original images. At first BRISQUE score was meant to be used to pick the best image obtained from the BEMD and EEMD filtration, but, as it will be described below, it was found out that for these images the BRISQUE score is not suitable.

4.3 Empirical mode decomposition implementation

EMD was tested in two versions - simple bi-dimensional EMD and its ensemble variation. Both algorithms differ only in the addition of one extra for cycle in EEMD, where the noise is added, and in the number of IMFs to be extracted.

4.3.1 Bi-dimensional empirical mode decomposition

Bi-dimensional EEMD algorithm is implemented in the `bidimensional_EMD` code. Chosen image is loaded into Matlab and then converted into double precision. Local extrema are found using Matlab functions `imregionalmax` and `imregionalmin`. Then extrema envelopes are defined using the `gridfit` interpolation function (downloaded from [33]). `Gridfit` offers more options for interpolation; for this application triangle interpolation was chosen, which is also the default. When having both extrema envelopes, their mean is counted. Mean is subtracted from the input image and then the stopping criterion for sifting process *SD* is obtained as:

$$SD = \frac{\sum\sum|(input - h)|^2}{\sum\sum(input)^2}, \tag{4.1}$$

where *input* is the input image and *h* is the difference between input image and mean envelope. If the condition *SD < 0.2* is fulfilled, *h* is marked the IMF and new *input* is defined as:

$$input = input - h; \tag{4.2}$$

and the process is repeated to obtain another IMF. In case that the condition is not fulfilled, new *input* is defined as:

$$input = h; \tag{4.3}$$

and the sifting process continues. When the number of maxima and minima in the actual input is less than defined threshold, sifting process is terminated completely and the rest of the input after the subtraction of the last IMF is marked as residue. This residue is added into one variable, named *IMF* along with all the IMFs, and in the following reconstruction is treated as IMF.

Filtered images are obtained by summing up all the IMFs plus residue, and subsequently one or two IMFs are subtracted. Also one image was reconstructed using only the first three IMFs. For each reconstructed image the BRISQUE score is obtained and the image is plotted along with this score. Another quality parameters that are computed are MSE, PSNR and SSIM. All filtered images are saved with their quality scores.

At first the algorithm was tested on model image. Obtained results are in Table 3. Input and filtered image are in the Fig. 18. According to the image, it can be said that BEMD partly removed the trend. SSIM and MSE values show that filtered image is very similar to the original.

Table 3.: BEMD results for model image filtration

image	original BRISQUE	IMFs	MSE	PSNR	SSIM	BRISQUE
model	65.053	-6. IMF	9.393E-04	30.272	0.994	65.603

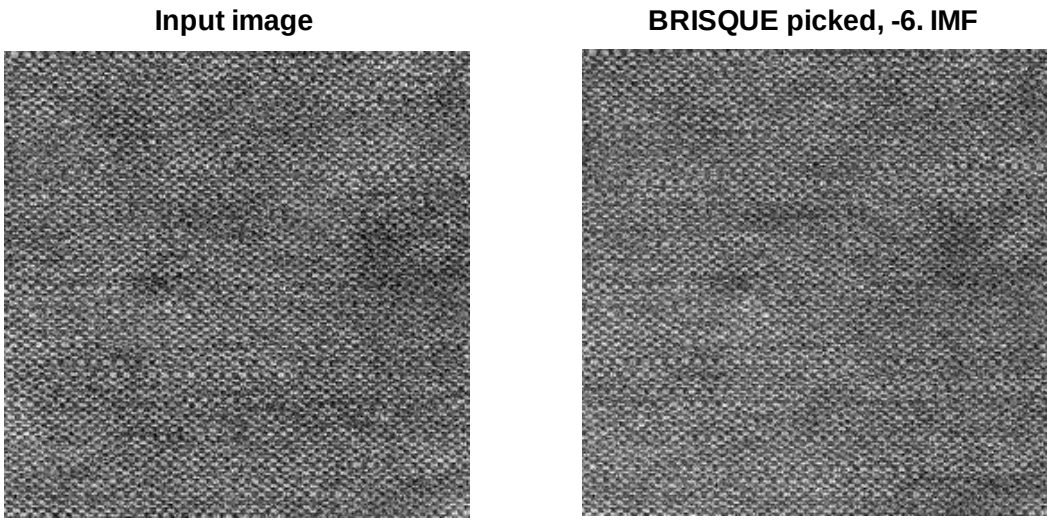

Fig. 18.: Model data - BEMD; original (left) and filtered image (right)

4.3.2 Ensemble empirical mode decomposition

As it was mentioned above, the internal EMD algorithm for EEMD is the same as in the BEMD algorithm, described in 4.3.1. Corresponding script is named `ensemble_EMD`. The number of noise realizations is set as 20. In each step the input image is noised with different realization of gaussian white noise using the `imnoise` function. For the noise parameters the default setting was used - noise is zero-mean with the variance of 0.01. The number of maxima and minima, acting as a threshold for terminating the whole sifting process, is defined depending on the image type - after running the script a dialog box asks user to choose whether the image is HR STEM or not. Then, for HR STEM images the number of IMFs to be extracted is set as 5, and for the others it is set as 4. This is ensured by dialogue window which appears after running the script.

Considering that the computation time rises almost exponentially along with the size of filtered image, another change was made in the script. To shorten the computation time, in each step the noised image is divided into patches of size 256 x 256 and after obtaining patch IMFs the filtered image is composed together. The reconstruction of filtered images is implemented in the same way as in the BEMD algorithm.

When applied to the model image, EEMD quite well removes the trend, caused by different thickness of the sample. Obtained results are in the Table 4; input and filtered image in the Fig. 19.

Table 4.: EEMD results for model image filtration

image	original BRISQUE	IMFs	MSE	PSNR	SSIM	BRISQUE
model	65.053	-4. IMF	8.669E-04	30.621	0.990	64.191

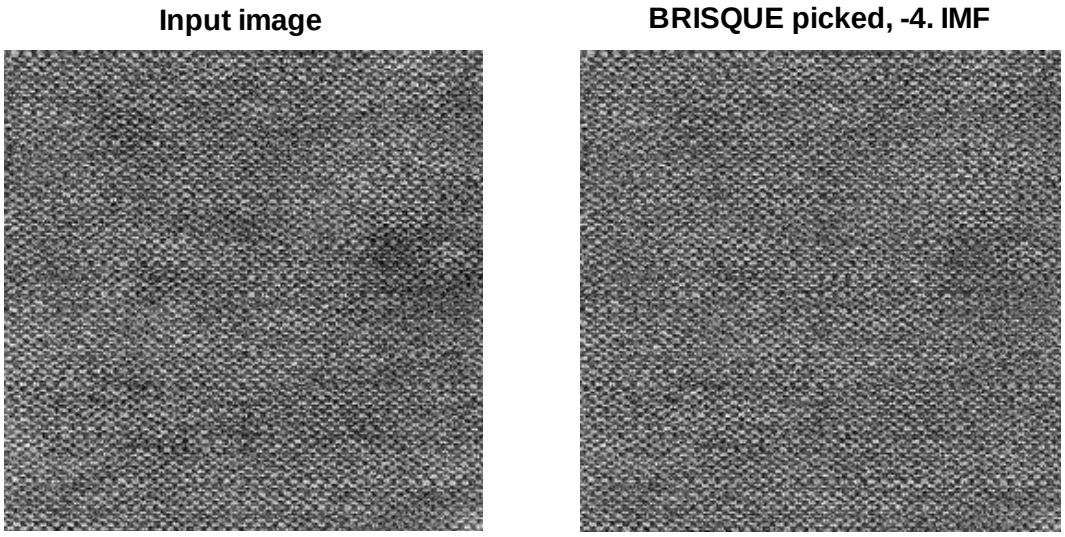

Fig. 19.: Model data - EEMD; original (left) and filtered image (right)

4.4 Singular value decomposition implementation

The singular value decomposition is realized via Matlab function `svd`. It decomposes input image into 3 matrices - *U*, *V* and *S*; where *U* is matrix with right eigenvectors, *V* is matrix containing left eigenvectors and *S* is pseudodiagonal matrix with singular values. This function is incorporated in script `SVD_filtration`. After the image is loaded into Matlab, a dialog box appears and asks for answer whether the image is STEM or not.

Threshold for erasing singular values was taken from the paper [30]:

$$threshold = \sigma\sqrt{2 \cdot \log(p)}; \tag{4.4}$$

where σ marks standard deviation and p marks width of the decomposed matrix. In this case image was divided into patches 256 x 256 px, thus p = 256.

However, this threshold proved to be too small for HR STEM images. To obtain threshold for these images, the length of the vector containing singular values was divided by 1.5 and from the singular values below this number their mean was computed. This threshold is purely experimental, and it was established on the visual assessment of the filtered images. During the testing it was also revealed that these STEM images have the noise contained in the first singular value, so this one was zeroed too. After the singular values are modified, filtered images are made using inverse SVD.

For each filtered image 4 quality scores are computed - MSE, PSNR, SSIM and BRISQUE score. Both original and filtered image are displayed in one figure along with BRISQUE score. Filtered image and its quality scores are saved in one cell array.

SVD filtration of the model data was able to suppress high-frequency noise. However, the vibration noise is still present. The influence of sample thickness was lowered a little. The results are in the Table 5; filtered result is in the Fig. 20.

Table 5.: SVD results for model image filtration

image	original BRISQUE	BRISQUE	MSE	PSNR	SSIM
model	65.053	66.419	1.161E-02	19.350	0.787

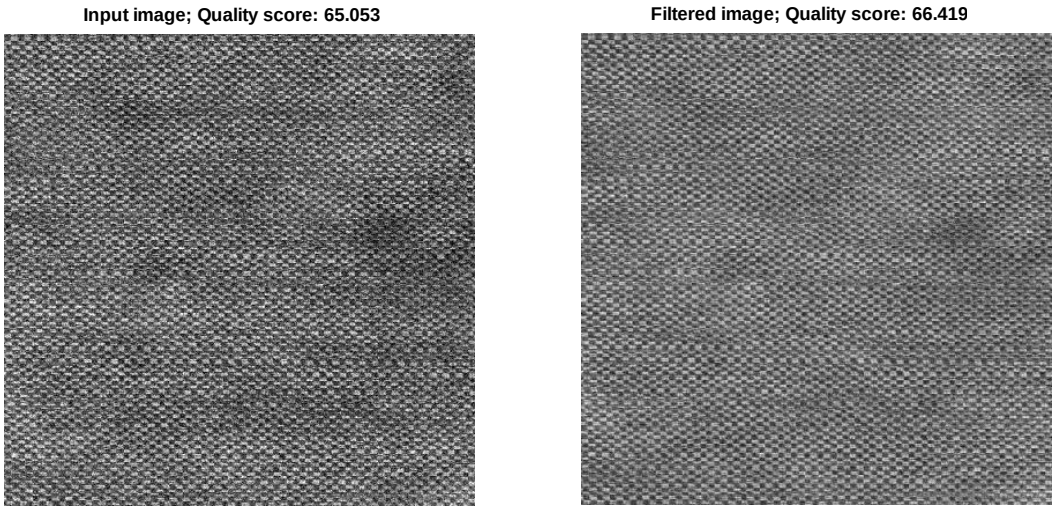

Fig. 20.: Model data - SVD; original (left) and filtered image (right)

4.5 Independent component analysis implementation

For the testing of ICA denoising method an ICALAB program [1] was used. ICALAB is activated by typing "icalab" in the Matlab Command window. Images are loaded by the "LOAD IMAGES" button. Then the scanning method and matrix type are chosen. Algorithm type is picked from the drop down list below. For this application methods SOBI-RO (SOBI with robust orthogonalization) algorithm was used. Button "RUN ALGORITHM" starts the estimation process. The obtained results (estimated components) can be plotted by pressing the button "PLOT". Checkboxes on the right side of this block serve to pick which data will be plotted or saved. The chosen data is then saved by pressing the button "SAVE". ICALAB is closed with the button "EXIT".

Script `ICA_filtration` serves to assess the estimated images quality. At first, original input image is loaded, then estimated images are loaded. ICALAB always saves estimated sources and their inverted version too, thus there is twice as much estimated images than the number of input images. For the quality assessment only the sources without "inv" in their name should be picked. All the chosen images are loaded into Matlab and for each of them BRISQUE score, MSE, PSNR and SSIM are computed. Each image is plotted along with the BRISQUE score value.

At first ICA was applied to the model image. Obtained results are in the Table 6. From the results in Fig. 21 it can be said that ICA was not very successful in this filtration. More testing results are in the chapter 5.3.

Table 6.: ICA results for model image filtration

image	original BRISQUE	BRISQUE	MSE	PSNR	SSIM
model	65.053	68.546	4.625E-02	13.349	0.589

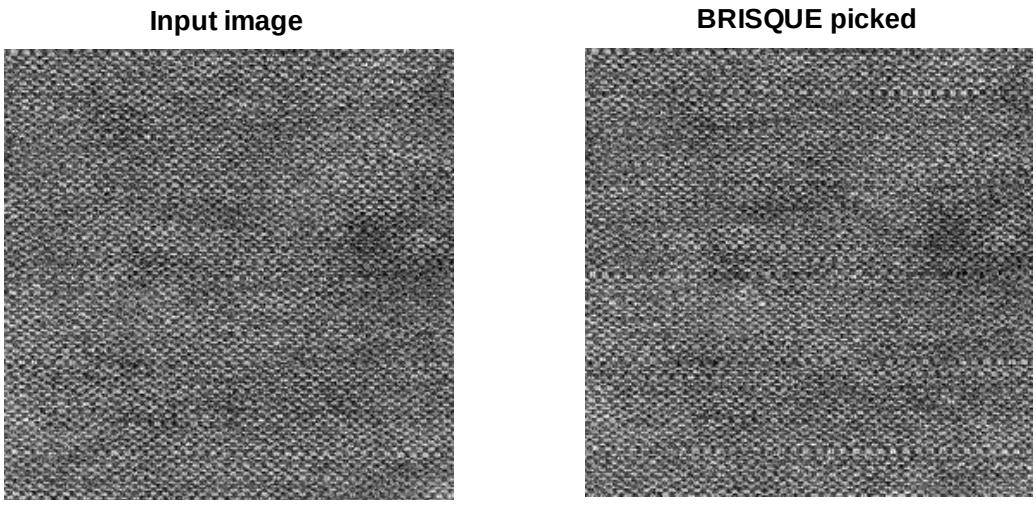

Fig. 21.: Model data - ICA, original (left) and filtered image (right)

5. Results

The following section contains results of all four filtering methods, and comparison between them. Also there are results obtained from median filter, average filter and filtration in the image spectrum.

5.1 Empirical mode decomposition results

The original idea of EMD filtration was to compare BRISQUE scores of all the obtained reconstructed images and then pick one with the best score. However, as it was already mentioned in the paragraph 4.2, BRISQUE has not proved to be applicable on these images. The best score was in some cases obtained for the images which either resembled to the noise than to the best filtered image. Also, TEM images are quite specific, thus for some applications qualitatively worse image could be more suitable, than one of high quality. Considering possible subsequent usage of these images for research, BRISQUE score is not suitable for the choice, because chosen images are often diagnostically useless. For that reason, the best filtered image was also picked manually, based on subjective visual empirical assessment; for both BEMD and EEMD.

For some images, subjective and objective choice were not that different. In subjective choice it was sometimes difficult decision between an image with completely subtracted trend or an image where high-frequency texture was well preserved. Subjective choice of some HAADF best-filtered images might seem wrong, because chosen images are blurred. However, these images were chosen on purpose, as they are free from the noise vibrations, formed during acquisition; e.g. human speech, walking, coughing. An example of this noise is in the Fig. 22. Also in these not very sharp images the dumbbell structure of Si is more distinguishable.

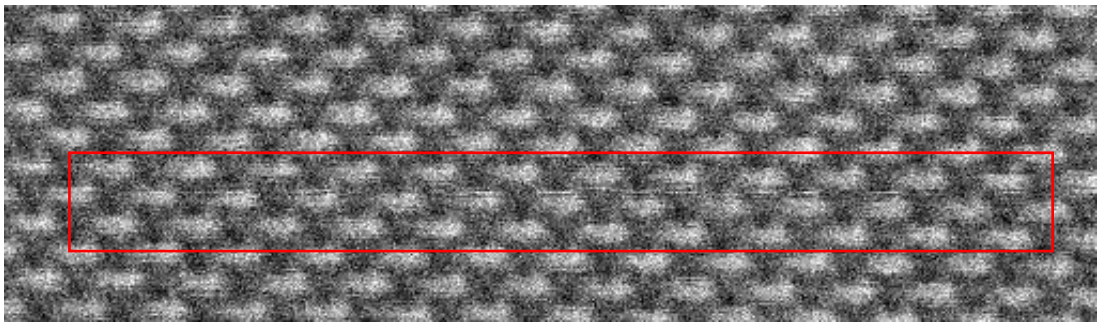

Fig. 22.: Image HAADF7, detail: Example of noise

5.1.1 Bi-dimensional ensemble mode decomposition

Using BEMD, all the images, except Zn2, were decomposed into 6 IMFs and residue. Results of both, objectively and subjectively picked best filtered images, are summarized in the Table 7. The first column contains images' names, the second contains BRISQUE scores of original data. Columns named "IMFs" contain the indices of IMFs excluded from the reconstruction - except for value "1st, 2nd and 3rd IMF", which marks the image composed using only the first three IMFs. Columns named "BRISQUE" contain BRISQUE scores for objectively and subjectively picked results.

Table 7.: BEMD filtration results

		BRISQUE picked		subjectively picked	
name	original BRISQUE	IMFs	BRISQUE	IMFs	BRISQUE
azbest3	75.501	-3. and 5. IMF	76.817	-6. IMF and residue	70.201
carbon2	79.153	-3. IMF and residue	77.103	- residue	69.460
feritic6	77.908	1st, 2nd, 3rd IMF	75.154	-4. IMF and residue	72.133
gold_X	153.580	-1. and 2. IMF	116.409	-5. IMF and residue	153.591
HAADF3	71.473	-2. IMF and residue	64.621	-5. IMF and residue	72.279
HAADF4	71.880	-2. IMF and residue	65.015	-6. IMF and residue	71.907
HAADF5	73.398	-2. and 4. IMF	65.960	-5. IMF and residue	71.272
HAADF6	71.857	- residue	72.018	-1. IMF and residue	100.276
HAADF7	69.449	-2. and 3. IMF	67.826	-6. IMF and residue	68.893
HAADF8	66.889	-2. and 5. IMF	66.569	1st, 2nd, 3rd IMF	65.727
HAADF9	73.259	-2. and 6. IMF	69.226	-5. IMF and residue	73.023
HAADF10	70.178	-2. IMF and residue	63.817	-4. IMF and residue	71.387
spinel2	76.803	-2. and 5. IMF	71.549	1st, 2nd, 3rd IMF	76.541
Zn2	116.228	-1. IMF and residue	116.060	-2. and 3. IMF	116.299
ZnS14	81.203	-2. and 3. IMF	78.152	-4. and 5. IMF	81.208

Image gold_X is an example of image, where BRISQUE score is inapplicable. The best score was obtained for the reconstruction, which does not even resemble to the original image. For the image Zn2, BRISQUE score also failed. Another example is image HAADF6, which is an image where blurred reconstruction was chosen subjectively. Filtered results are in Fig. 24, Fig. 26 and Fig. 28. For the other images the difference between objectively and subjectively picket images was not so significant. Image spinel2 is an example of filtration (subjective choice), where the influence of sample thickness was quite well suppressed (Fig. 30).

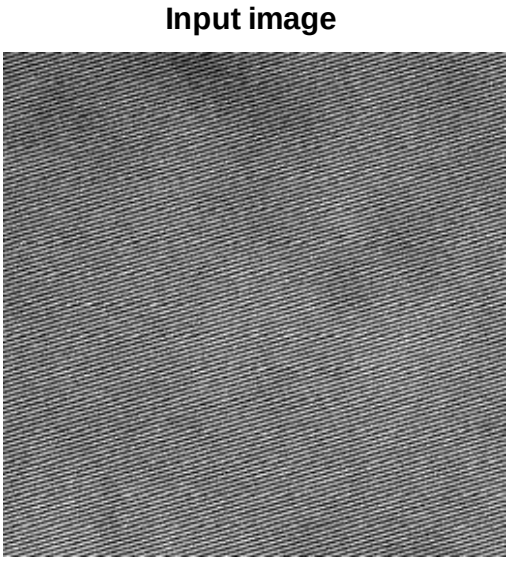

Fig. 23.: Gold_X; original image

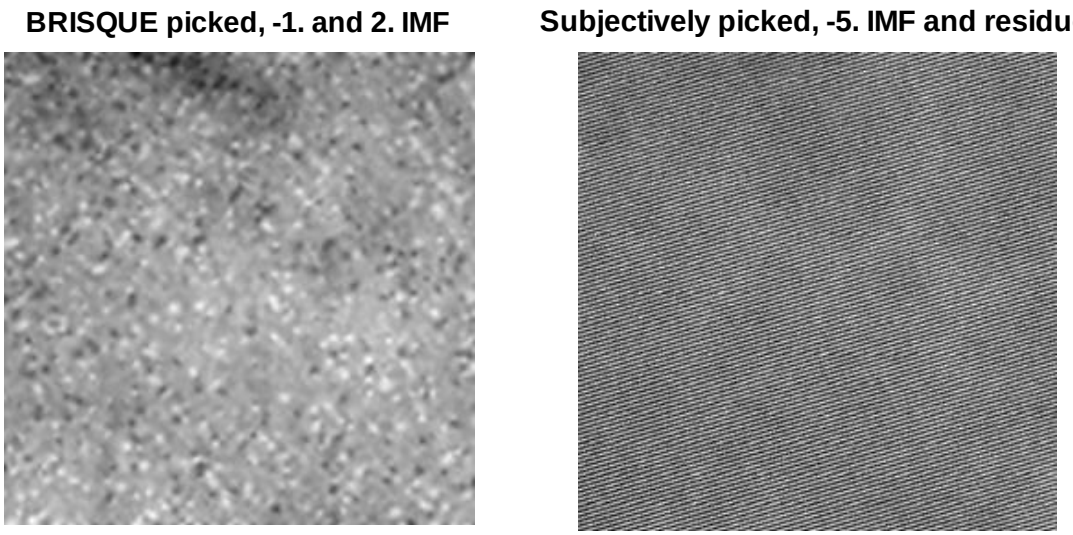

Fig. 24.: Gold_X BEMD filtered; objectively (left) and subjectively (right) picked image

Fig. 25.: Zn2; original image

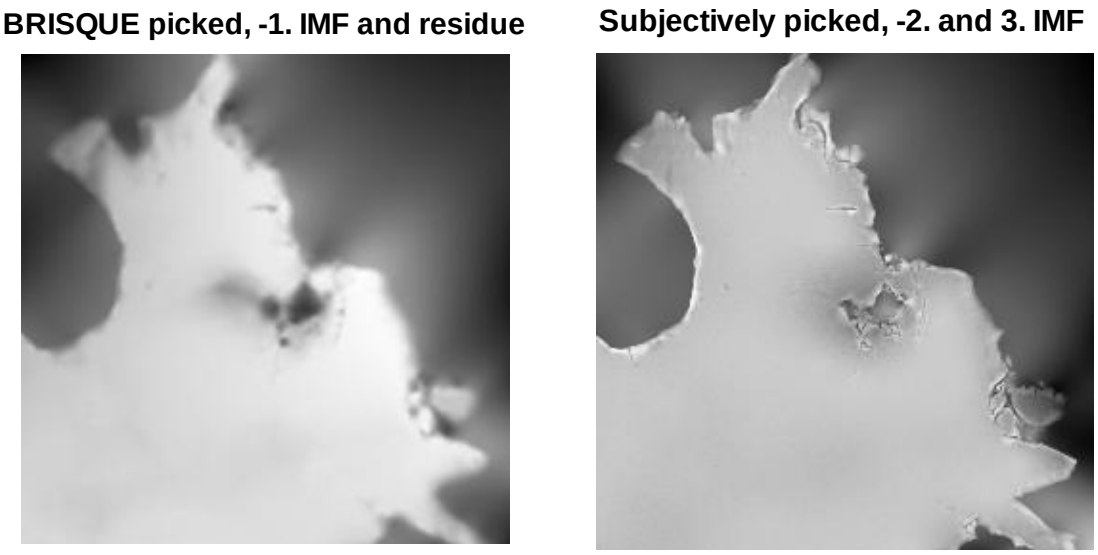

Fig. 26.: Zn2 BEMD filtered; objectively (left) and subjectively (right) picked image

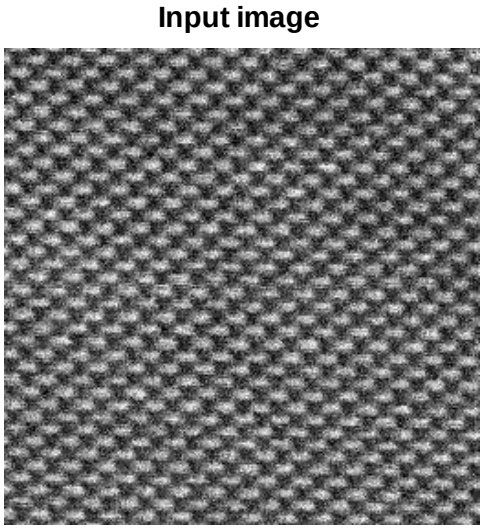

Fig. 27.: HAADF6; original image

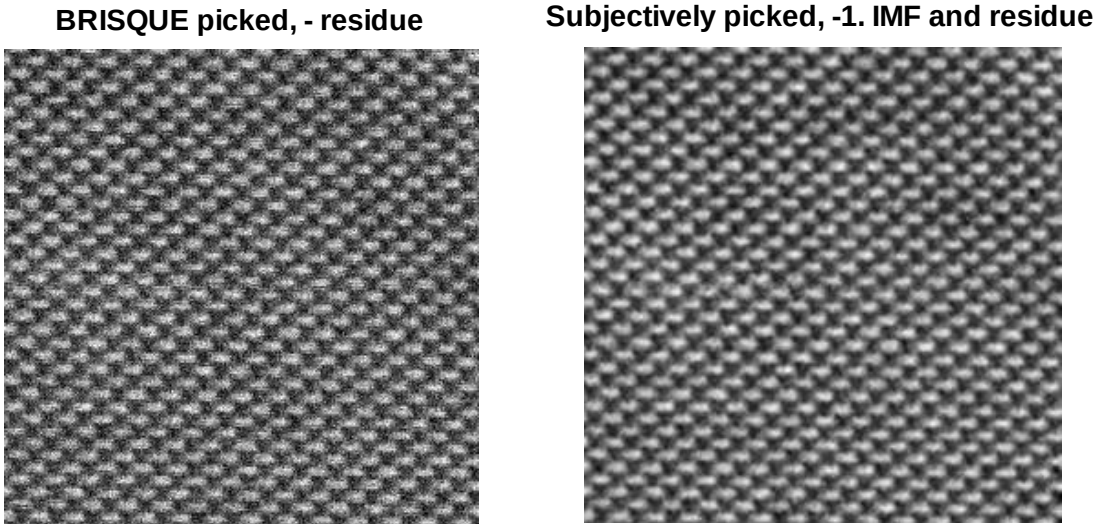

Fig. 28.: HAADF6 BEMD filtered; objectively (left) and subjectively (right) picked image

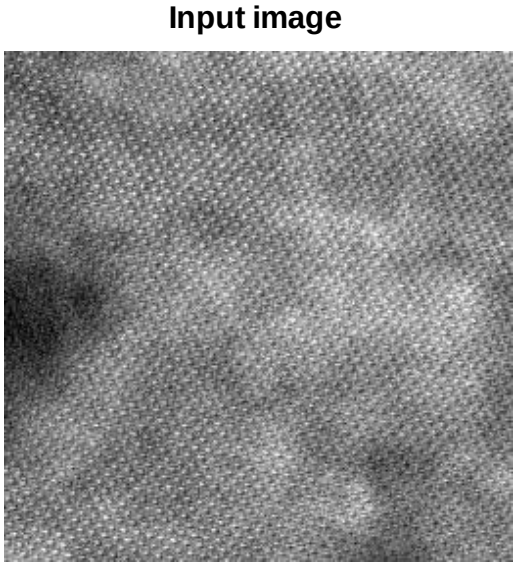

Fig. 29.: Spinel2; original image

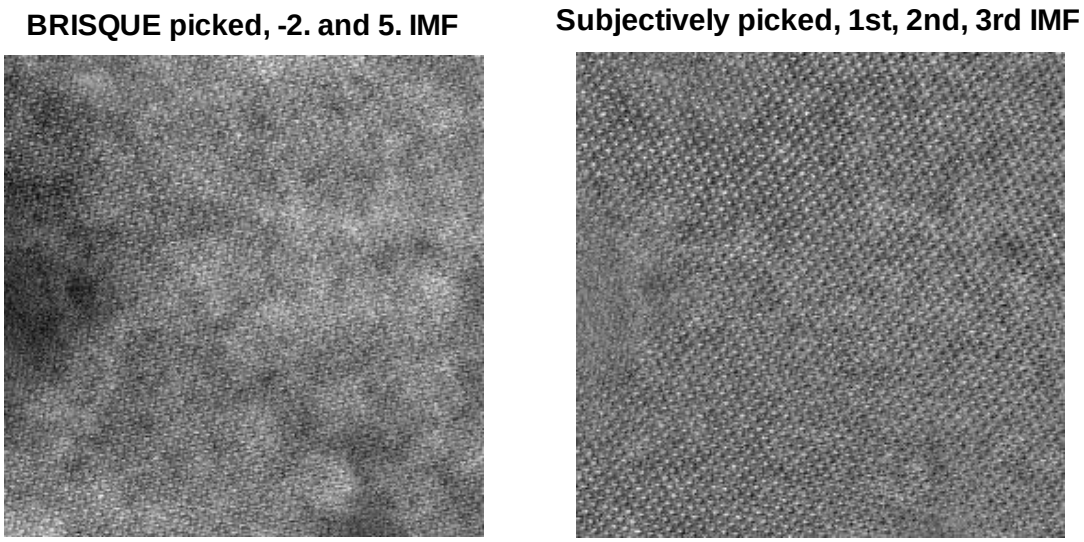

Fig. 30.: Spinel2 BEMD filtered; objectively (left) and subjectively (right) picked image

5.1.2 Ensemble empirical mode decomposition

Filtered images obtained from EEMD filtration were visually slightly influenced by the separation into 256 x 256 px subimages, due to the time consuming processing. This happened because the number of image extremas was declining along with the rising number of IMFs. Due to that, the subIMFs with higher number did not complement each other good enough. This influence appeared when the first and/or the second IMFs were excluded from the reconstruction. Fortunately, visible distortion is present only in a few reconstructed images, as the last IMFs and residue were usually excluded.

The results from EEMD filtration are in the Table 8. Columns named "IMFs" contain the indices of IMFs excluded from the reconstruction; only the value "1st, 2nd and 3rd IMF", marks that the image composed using only the first three IMFs. Columns named "BRISQUE" contain BRISQUE scores for objectively and subjectively picked results.

Table 8.: EEMD filtration results

EEMD		BRISQUE picked		subjectively picked	
image	original BRISQUE	IMFs	BRISQUE	IMFs	BRISQUE
azbest3	75.501	-2. and 3. IMF	69.023	- residue	76.345
carbon2	79.153	-3. and 4. IMF	71.348	-3. IMF and residue	73.461
feritic6	77.908	-2. and 4. IMF	69.373	-4. IMF	73.884
gold_X	153.580	-1. and 4. IMF	104.268	1st, 2nd, 3rd IMF	153.569
HAADF3	71.473	-2. and 5. IMF	63.436	-3. IMF and residue	70.621
HAADF4	71.880	-2. and 5. IMF	63.500	-1. and 5. IMF	100.640
HAADF5	73.398	-2. and 3. IMF	64.199	-1. IMF and residue	101.336
HAADF6	71.857	-5. IMF	71.639	-1. IMF and residue	118.140
HAADF7	69.449	-2. and 4. IMF	67.777	-1. and 5. IMF	113.036
HAADF8	66.889	-2. IMF and residue	65.328	-4. IMF and residue	65.829
HAADF9	73.259	-2. and 5. IMF	67.513	-3. IMF and residue	72.332
HAADF10	70.178	-2. and 3. IMF	62.335	-4. IMF and residue	69.552
spinel2	76.803	-2. and 3. IMF	69.214	-3. and 4. IMF	73.148
Zn2	116.228	-1. and 2. IMF	116.104	-3. IMF and residue	117.507
ZnS14	81.203	-2. and 3. IMF	73.997	-3. and 4. IMF	78.166

For the images HAADF4, HAADF5, HAADF6 and HAADF7 were subjectively chosen their blurred reconstructions; that is why their BRISQUE score differs that much from objectively picked ones. Image Zn2 is corrupted the most with the influence of the segmentation into subimages. Both its filtered results are in the Fig. 32.

Fig. 31.: Zn2; original image

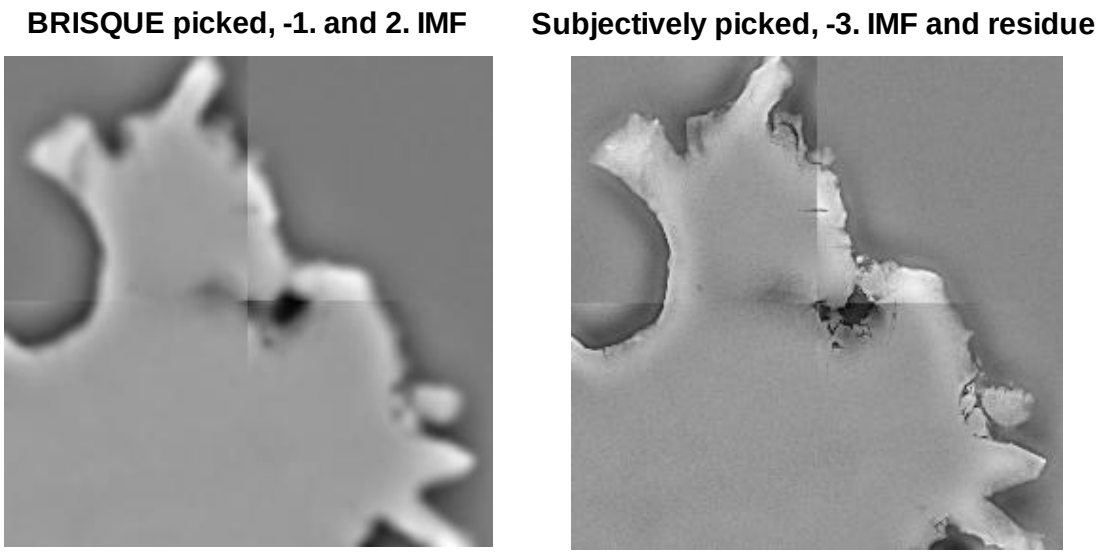

Fig. 32.: Zn2 EEMD filtered; objectively (left) and subjectively (right) picked image

When comparing BRISQUE scores for both BEMD and EEMD it is obvious that EEMD BRISQUE scores are significantly lower. Generally it can be said that usage of twenty different noisy realizations and averaging them brings better results than simple BEMD without noise.

5.2 Singular value decomposition results

SVD, unlike the EMD algorithms, was computationally very fast; even for larger images (1024 x 1024 px). For each input image only one filtered version was obtained. All the results are summarized in the Table 9 below.

Table 9.: SVD filtration results

image	original BRISQUE	BRISQUE	MSE	PSNR	SSIM
azbest3	75.501	75.728	1.552E-02	18.092	0.709
carbon2	79.153	79.153	2.499E-07	66.023	1.000
feritic6	77.908	77.867	5.096E-07	62.928	1.000
gold_X	153.580	153.580	1.182E-08	79.274	1.000
HAADF3	71.473	74.513	1.040E-02	19.829	0.787
HAADF4	71.880	76.986	1.025E-02	19.892	0.762
HAADF5	73.398	80.011	1.030E-02	19.872	0.781
HAADF6	71.857	86.021	1.085E-02	19.645	0.645
HAADF7	69.449	79.627	1.090E-02	19.627	0.641
HAADF8	66.889	71.185	1.509E-02	18.214	0.681
HAADF9	73.259	78.861	9.753E-03	20.109	0.806
HAADF10	70.178	72.702	1.066E-02	19.724	0.750
spinel2	76.803	76.803	1.049E-07	69.791	1.000
Zn2	116.228	116.187	7.003E-05	41.547	0.965
ZnS14	81.203	81.202	1.847E-07	67.335	1.000

According to the MSE and SSIM values of the first 7 images, it can be said that this filtration was not very successful. These images were filtered using threshold from the paper [30]. However, larger thresholds for zeroing singular values caused the loss of images' texture. An example of SVD filtered image is in the Fig. 33.

For the HR STEM images the applied threshold was different. As they have periodic texture, the image information is contained in smaller number of singular values with higher values. Also, dependent on the magnification of the image during acquisition and its final size, main spatial frequencies are lower. Thanks to that it was also found out that by zeroing the first singular value the high-frequency noise is removed from the image. This leads to the filtered images being a little blurred, but visually they look better and they can be easily processed in possible further analyses. An example of filtered HR STEM image is in Fig. 34.

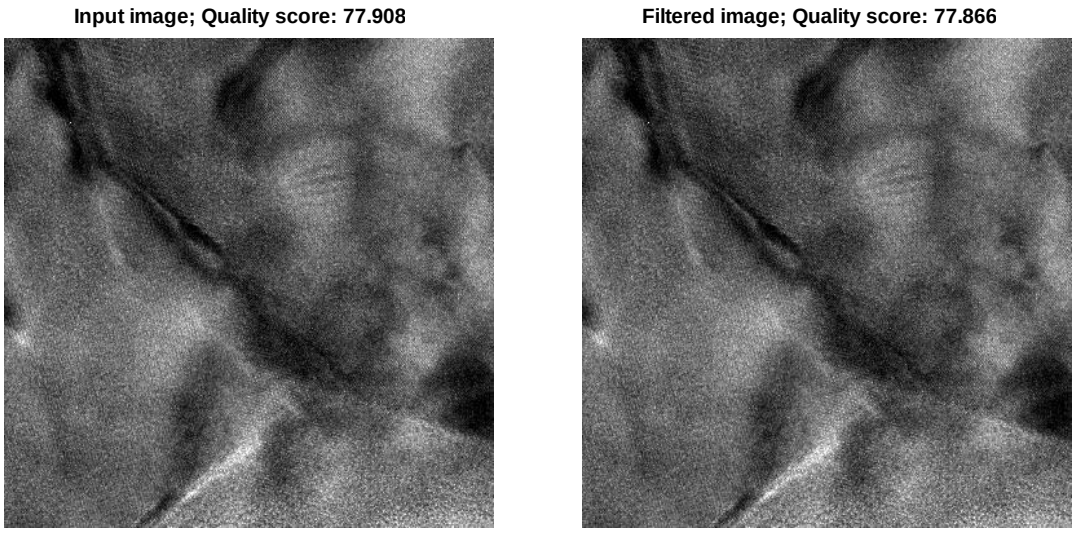

Fig. 33.: Image feritic6; original (left) and filtered with SVD (right)

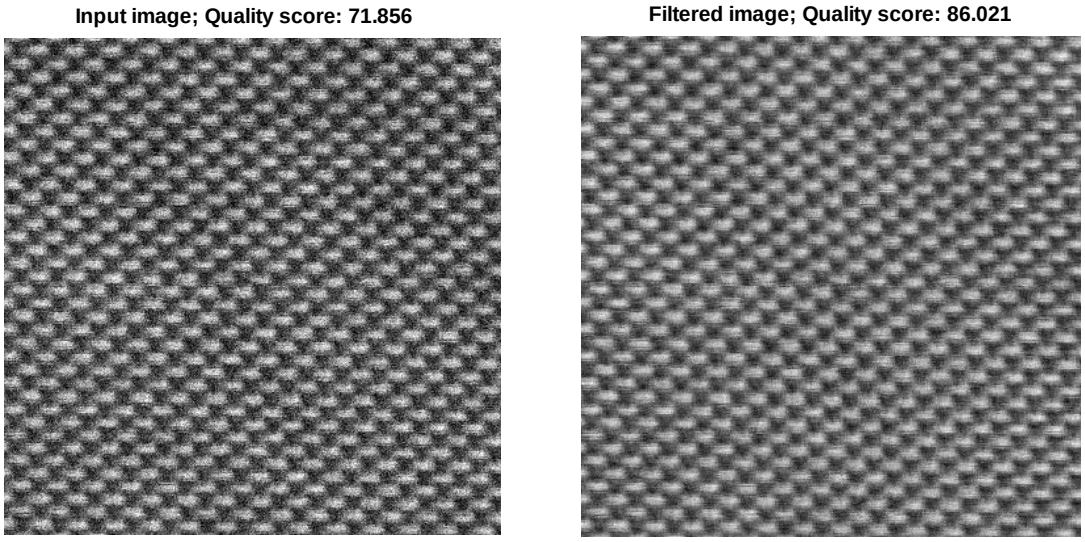

Fig. 34.: Image HAADF6; original (left) and filtered with SVD (right)

5.3 Independent component analysis results

ICA was tested in multiple ways, however neither one proved to bring results. One idea was to use several BF or DF images taken from the same area of specimen and try to estimate result by filtering out all the noise. This idea turned out to be inapplicable due to the drift of the specimen - though the acquisition parameters were still the same, the specimen moved itself. The second idea was to corrupt input image with two different realizations of gaussian noise and then use them as inputs along with three identical original images. This method failed too because ICA only estimated matrix with added noise and original image stayed unfiltered.

The third approach was to use just 5 identical original images as input. In this method ICA estimated 5 sources only from original data. The fifth estimated source always contained original image, the others were different. However, when comparing obtained estimated sources it turned out that neither this approach managed to filter out the noise. For HR STEM images this approach failed completely, no noise was removed. For the other images the results were a little better but still this method cannot be considered as applicable for TEM images. Obtained best results, based on BRISQUE score and also subjectively chosen, are in the Table 10.

Table 10.: ICA filtration results

		BRISQUE picked		Subjectively picked	
image	original BRISQUE	estimated source	BRISQUE	estimated source	BRISQUE
azbest3	75.501	estimated image 2	79.760	estimated image 1	86.511
carbon2	79.153	estimated image 4	79.058	estimated image 3	86.318
feritic6	77.908	estimated image 3	81.024	estimated image 1	89.653
gold_X	153.580	estimated image 2	84.770	estimated image 1	153.476
HAADF3	71.473	estimated image 2	74.418	estimated image 2	74.418
HAADF4	71.880	estimated image 1	74.801	estimated image 1	74.801
HAADF5	73.398	estimated image 2	75.526	estimated image 2	75.526
HAADF6	71.857	estimated image 1	74.211	estimated image 1	74.211
HAADF7	69.449	estimated image 1	72.628	estimated image 1	72.628
HAADF8	66.889	estimated image 2	70.684	estimated image 2	70.684
HAADF9	73.259	estimated image 2	73.942	estimated image 2	73.942
HAADF10	70.178	estimated image 4	72.523	estimated image 2	73.440
spinel2	76.803	estimated image 2	77.632	estimated image 1	77.797
Zn2	116.228	estimated image 2	80.535	estimated image 1	116.175
ZnS14	81.203	estimated image 2	81.920	estimated image 1	90.746

Carbon2 is the only image from which this method managed to separate its components. Filtered results are in the Fig. 36. Subjectively picked image looks like quite good representation of image's texture. Objectively picked image resembles more to the noise. Some of the best-score estimated sources looked just the same as the input image, but when both images were zoomed, estimated image only contained doubled pixels with the same intensity. This difference is pictured in the Fig. 37.

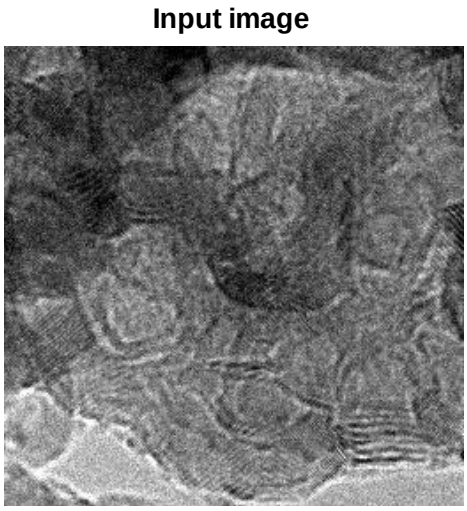

Fig. 35.: Carbon2; original image

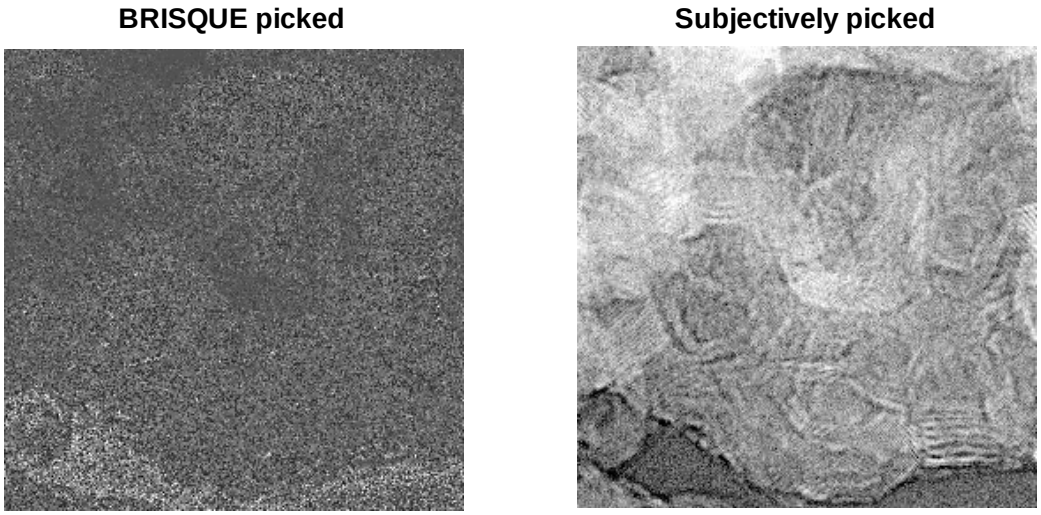

Fig. 36.: Carbon2 ICA filtered; objectively (left) and subjectively (right) picked image

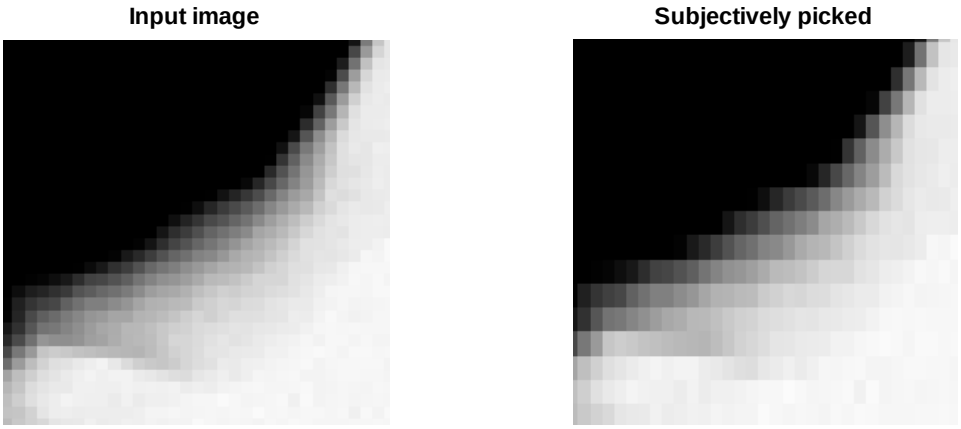

Fig. 37.: Zn2 image - detail; original (left) and ICA filtered (right) image

5.4 Commercial methods for comparison

To compare the results of this work with normally used ones, median and averaging filter were chosen. [26] Both were realized via Matlab functions - `medfilt2` and `fspecial` with parameter `'average'` and size 3. The third applied method was zeroing of the DC component via Fourier's spectrum of the image. [37]. BRISQUE scores for each image and all three methods are presented in the Table 11.

Table 11.: Median, averaging and spectral filtering - results

	original	median	average	spectral filtering
image	BRISQUE			
azbest3	75.501	97.685	87.029	72.307
carbon2	79.153	107.250	92.728	69.620
feritic6	77.908	101.454	92.758	76.257
gold_X	153.580	153.591	153.591	111.045
HAADF3	71.473	83.625	82.766	72.905
HAADF4	71.880	82.624	80.923	75.326
HAADF5	73.398	82.724	78.479	74.756
HAADF6	71.857	89.672	86.677	66.092
HAADF7	69.449	85.064	82.975	65.392
HAADF8	66.889	77.676	72.403	71.235
HAADF9	73.259	83.504	80.937	70.973
HAADF10	70.178	82.115	81.066	69.334
spinel2	76.803	93.291	89.916	84.624
Zn2	116.228	116.029	116.296	116.352
Zn14	81.203	84.429	83.895	83.813

In general, both median and averaging filter visually proved quite well removal of the high frequency noise in HR STEM images. They also suppressed vibration noise. An example is in the Fig. 38. On the other hand, neither one of those filters managed to remove the trend, i.e. the noise caused by the different sample's thickness. As they filter the image via sliding window, they also cause data loss or they create false data in the edges of image, dependent on the size of the window. However, those filters did not prove to be suitable for images without periodic texture (Fig. 39).

Filtration via zeroing in the spectrum, on the other hand, brought interesting results for non-periodic images. Though most obtained images were very dark, this filter highlighted the textural details. The most interesting result via this filtration was the one obtained for Zn2 image. All the details on the edges are very well distinguishable (Fig. 40).

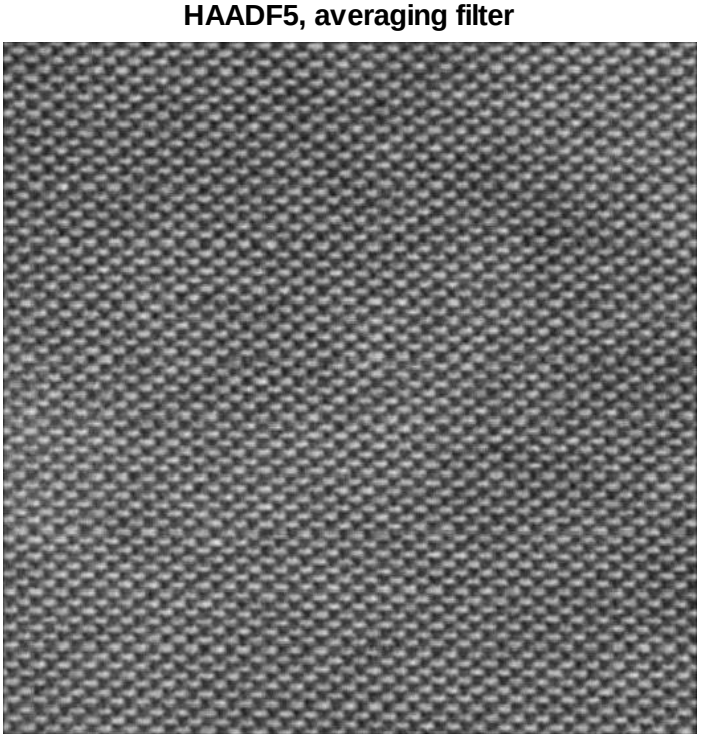

Fig. 38.: HAADF5; averaging filtration

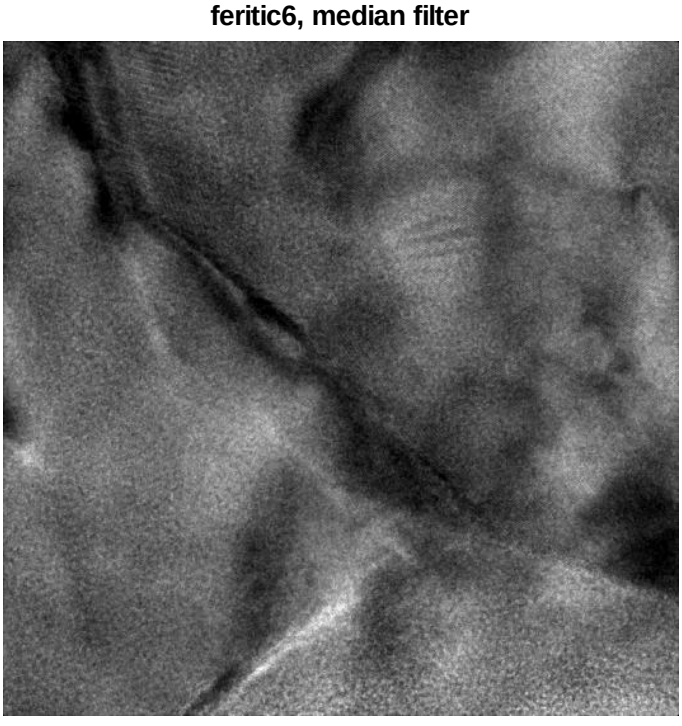

Fig. 39.: Feritic6, median filtration

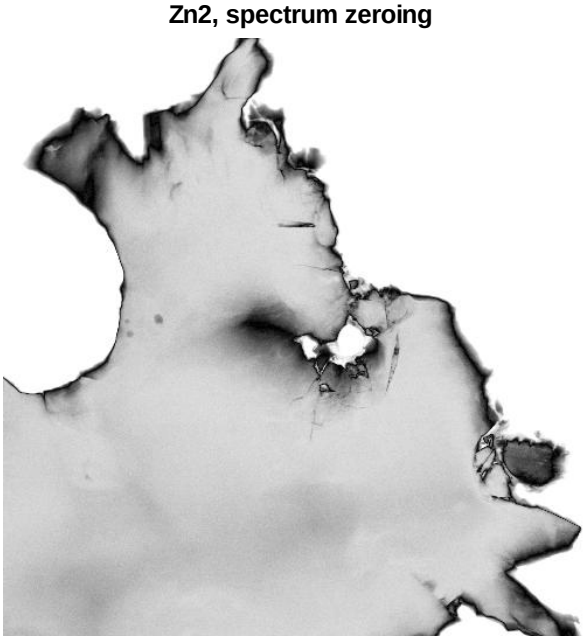

Fig. 40.: Zn2; filtration in the spectrum

5.5 Discussion

Four image filtration methods were implemented in this work. Two variations on EMD turned out to provide quite good trend removal while preserving details at the same time; though EEMD is a little better. They are both able to remove vibration noise from the image. EEMD filtration has generally better results thanks to the usage of different noise realizations and averaging them. EEMD also provides better results for HR STEM images with smaller magnification. The smaller is magnification the more difficult is to filter out high frequency noise, as the image texture frequency rises. On the other hand, BEMD is considerably faster as it is concerned to the computation time, and do not suffer from distortion caused by segmentation.

Filtering out the trend using EEMD was visually the most successful for images azbest3 (Fig. 41), carbon2 (Fig. 42) and spinel2 (Fig. 43). In all three images the details are preserved, while uneven intensities in the background were removed. On the other hand, image Zn2 was distorted the most due to the segmentation of image during filtration (Fig. 32, right subimage).

As it was mentioned above, BEMD filtration was slightly worse. It was not able to remove high-frequency noise from HR STEM images with smaller magnification without blurring them too much. The main advantage of BEMD, compared to EEMD, is still the computation time and the filtration of whole image without segmentation. The choice between these two methods depends on, whether better results or faster computation is preferred.

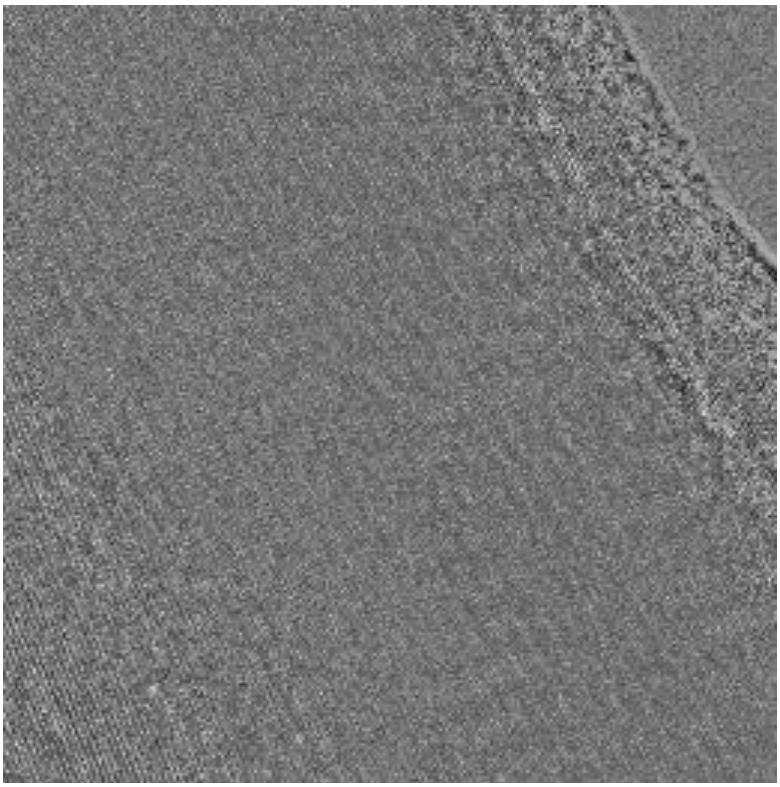

Fig. 41.: Azbest3, EEMD filtration result

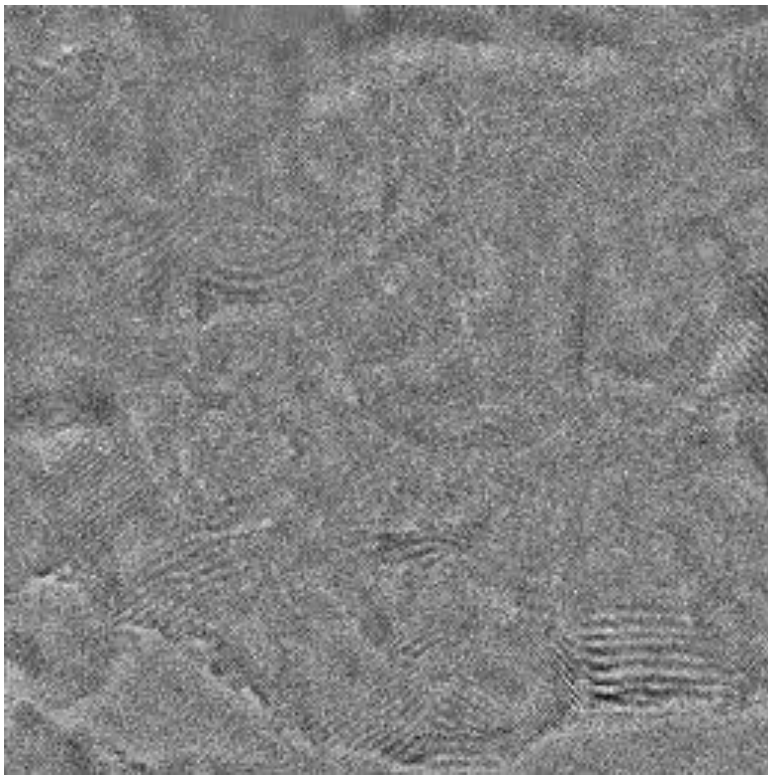

Fig. 42.: Carbon2, EEMD filtration result

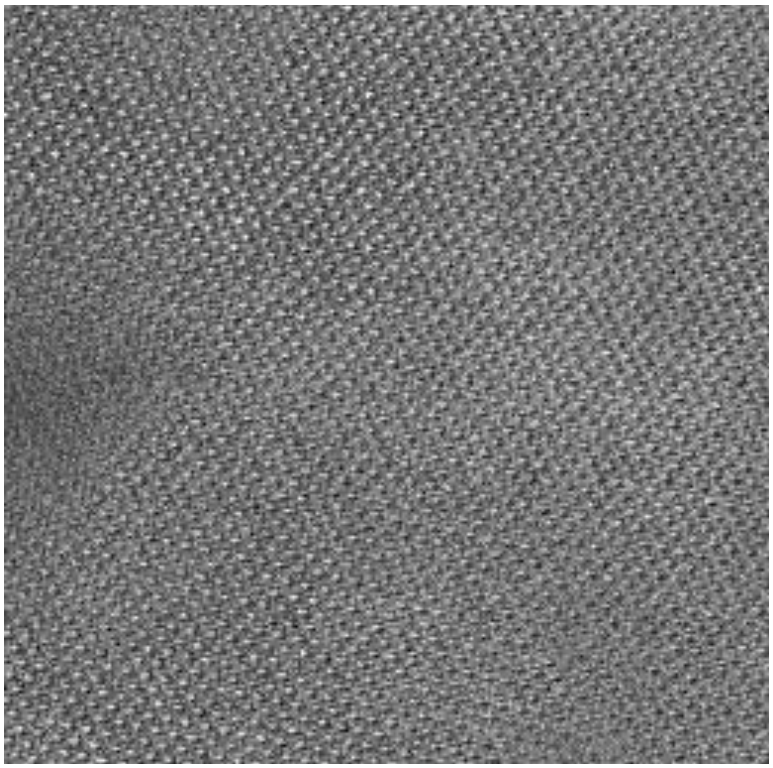

Fig. 43.: Spinel2, EEMD filtration result

The SVD filtration did not performed well on non-periodic texture images. Obtained filtered images were almost the same as input ones. Due to their texture it was not possible to find universal adaptive threshold for zeroing singular values, and threshold mentioned in [30] was too small. In relation to this work it can be said that SVD is not suitable for filtering this type of images. On the other hand, it has proved to be quite useful for filtering HR STEM images. Proposed empirical threshold along with zeroing the first singular value has given satisfying results. Compared to EMD results, SVD filtered HR STEM images are sharper, but still individual dumbbells are slightly distinguishable. One disadvantage is that, unlike EMD, SVD was not able to filter out vibration noise. On the other hand, computation time of SVD filtration was very short compared to both BEMD and EEMD.

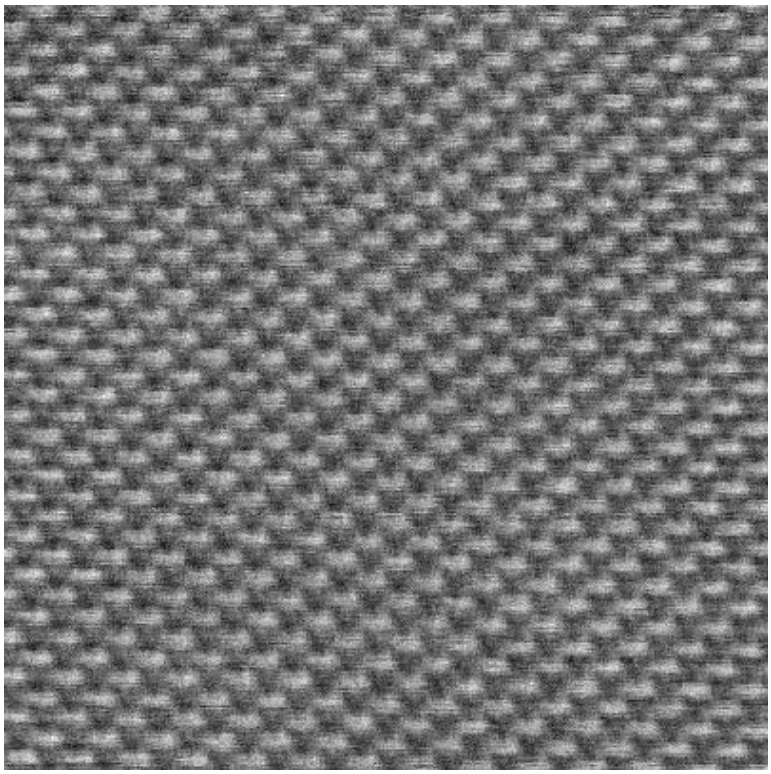

Fig. 44.: HAADF7, SVD filtration

The ICA filtration turned out to be inapplicable for these TEM images. The original idea to apply it on multiple images of the same area of specimen failed due to the sample drift. Adding several noise realizations to the same input image and then analyze them along with input images also did not work; only the added noise was separated without filtering the image. Using of five identical input images as five mixtures did not succeed as well. Also estimated images contained doubled pixels that could blur the results, which is presented in Fig. 37 (right subimage).

Commercially available methods, represented by the median and averaging filter and filtering in image's spectrum, were also tested on the whole image set. Median and averaging filter proved to be quite good for removing high-frequency noise from HR STEM images. Median filter is able to remove high-frequency noise without blurring image that much, compared to the other methods; but filtered image becomes less sharp with larger window size. Both filters removed vibration noise. On the other hand they are useless for non-periodic texture images and also they cannot suppress the influence of the specimen's uneven thickness. Zeroing in Fourier's spectrum provided better results for non-periodic images where it highlighted details in structure. However, obtained images were very dark.

6. Conclusion

The first chapter of this work is dedicated to the transmission electron microscope. The second chapter deals with the interaction of the electrons with observed specimen. Basic properties of electron are given here and several possible scattering events are described along with the conditions of their appearance. This chapter also includes the description of TEM and STEM imaging techniques.

In the third chapter there is an overview of chosen filtration techniques, especially those based on the image decomposition. The chosen decomposition methods are Empirical mode decomposition (EMD), Principal component analysis (PCA), Independent component analysis (ICA) and Singular value decomposition (SVD). Along with the methods, the examples of their application in actual research are presented. Finally, some image quality assessment methods, which were used to assess the filtration efficiency, are described.

The practical part deals with the application of described filtration methods. PCA was excluded from the filtration, because available methods assumed that images are corrupted with white noise, which does not correspond with the topic of this work. All the other methods were implemented in Matlab. Algorithms were tested on model image and then on image dataset, containing HR STEM images and TEM images. Obtained results are presented in the chapter 5. Due to the problems with image quality assessment algorithm BRISQUE, which turned out not to be suitable, the efficiency of filtration was partially subjectively assessed.

For EMD two separate versions were tested - bi-dimensional EMD (BEMD) and ensemble EMD (EEMD). BEMD algorithm is a lot faster, compared to the EEMD. Another advantage of BEMD is that it does not corrupt image due to the segmentation into subimages. Both BEMD and EEMD proved to be able to suppress the influence of sample's uneven thickness; however, EEMD removed this noise perceptibly better. These methods also managed to filter out high-frequency noise from HR STEM images with larger magnification, along with vibration noise which originates during acquisition. Images filtered this way are slightly blurred, but they can be easily used for further processing. According to the BRISQUE score, EEMD performed better thanks to the averaging of 20 noisy realizations of input image. On the other hand it is very time consuming method. It is also the reason why the input images were segmented into 256 x 256 subimages to be processed individually and then composed back.

The improvement in EEMD filtration results could be achieved with addition of more noise realizations in ensemble. Also distortion caused due to segmentation could be removed by filtering whole image, or usage of smaller sliding window from which only several central pixels would be used in the filtered image. All proposed improvements, have requirements on better hardware, as they are very computationally costly.

SVD filtration was realized with two thresholds for singular values zeroing; one is for HR STEM images and another for the non-periodic texture images. Originally the threshold from [30] was applied, but during testing it turned out that for HR STEM images its value is too low. Thus, the original threshold was kept for non-periodic texture images, as choosing of the adaptive threshold was unsuccessful. For HR STEM images empirical threshold was created. SVD did not proved to be suitable for filtering non-periodic images, but it performed well on HR STEM images. It successfully removed high-frequency noise, unfortunately it did not suppressed vibration noise.

From all the tested methods, ICA was found out to be the least suitable. After multiple series of testing it came out that this method was not able to remove noise from test images or decompose them into components usable for more processing. One possible option is to test this method on a set of TEM or STEM images acquired from the same area of specimen in very short period of time, before the specimen drift occurs. However, for the data used in this work, ICA was found to be inapplicable.

In conclusion, four blind filtration methods were tested in this work. Three of them are potentially suitable for TEM images filtration; namely bi-dimensional empirical decomposition, ensemble empirical decomposition and singular value decomposition. The last method did not proved to be suitable, but it might provide some usable results when applied to different data set. For all the tested methods there are possibilities of further research.

References

[1] A. Cichocki, S. Amari, K. Siwek, T. Tanaka , Anh Huy Phan et al., ICALAB Toolboxes, [accessed 2017-12-30]. Available at: http://www.bsp.brain.riken.jp/ICALAB

[2] A. Mittal, A. K. Moorthy and A. C. Bovik, "BRISQUE Software Release", URL: http://live.ece.utexas.edu/research/quality/BRISQUE_release.zip, 2011. [accessed 2018-03-26]

[3] AL-BADDAI, Saad, Karema AL-SUBARI, Ana Maria TOMÉ, Bernd LUDWIG, Diego SALAS-GONZALES and Elmar Wolfgang LANG. Analysis of fMRI images with bi-dimensional empirical mode decomposition based-on Green's functions. *Biomedical Signal Processing and Control* [online]. 2016, **30**, 53-63. DOI: 10.1016/j.bspc.2016.06.019. ISSN 17468094. Available at: http://linkinghub.elsevier.com/retrieve/pii/S1746809416300799

[4] AL-BADDAI, Saad, Karema AL-SUBARI, Ana Maria TOMÉ, Jordi SOLÉ-CASALS and Elmar Wolfgang LANG. A green's function-based Bi-dimensional empirical mode decomposition. *Information Sciences* [online]. 2016, **348**, 305-321. DOI: 10.1016/j.ins.2016.01.089. ISSN 00200255. Available at: http://linkinghub.elsevier.com/retrieve/pii/S0020025516300317

[5] Annular bright-field scanning transmission electron microscopy. In: *JEOL* [online]. [accessed. 2017-12-30]. Available at: https://www.jeol.co.jp/en/words/emterms/search_result.html?keyword=annular%20bright-field%20scanning%20transmission%20electron%20microscopy

[6] BAGHAIE, Ahmadreza, Roshan M. D'SOUZA and Zeyun YU. Application of Independent Component Analysis techniques in speckle noise reduction of retinal OCT images. *Optik - International Journal for Light and Electron Optics* [online]. 2016, **127**(15), 5783-5791. DOI: 10.1016/j.ijleo.2016.03.078. ISSN 00304026. Available at: http://linkinghub.elsevier.com/retrieve/pii/S0030402616302583

[7] ÇELEBI, Aysun Taşyapı and Sarp ERTÜRK. Visual enhancement of underwater images using Empirical Mode Decomposition. *Expert Systems with Applications* [online]. 2012, **39**(1), 800-805. DOI: 10.1016/j.eswa.2011.07.077. ISSN 09574174. Available at: http://linkinghub.elsevier.com/retrieve/pii/S0957417411010396

[8] CICHOCKI, Andrzej. and Shun'ichi. AMARI. *Adaptive blind signal and image processing: learning algorithms and applications*. Chichester: J. Wiley, c2002. 554 p. ISBN 04-716-0791-6.

[9] CHEN, Chao-Yu, Chin-Hsing CHEN, Chao-Ho CHEN and Kuo-Ping LIN. An automatic filtering convergence method for iterative impulse noise filters based on PSNR checking and filtered pixels detection. *Expert Systems with Applications* [online]. 2016, **63**, 198-207. DOI: 10.1016/j.eswa.2016.07.003. ISSN 09574174. Available at: http://linkinghub.elsevier.com/retrieve/pii/S0957417416303487

[10] CHEN, Chih-Sung and Yih JENG. Two-dimensional nonlinear geophysical data filtering using the multidimensional EEMD method. *Journal of Applied Geophysics* [online]. 2014, **111**, 256-270. DOI: 10.1016/j.jappgeo.2014.10.015. ISSN 09269851. Available at: http://linkinghub.elsevier.com/retrieve/pii/S0926985114003097

[11] Convergent beam diffraction pattern. In: *Warwick* [online]. [accessed 2017-12-30]. Available at: https://warwick.ac.uk/fac/sci/physics/research/condensedmatt/microscopy/research/researchthemes/d-ed/d-lacbed/d-lacbed_symmetry/

[12] Documentation. *MathWorks* [online]. Natick, Massachusetts: The MathWorks, c1994-2018 [accessed 2018-05-14]. Available at: https://www.mathworks.com/help/matlab/

[13] ENRI, Rolf. *Aberration-corrected imaging in transmission electron microscopy: an introduction* [online]. Hackensack, NJ: Distributed by World Scientific Pub. Co., c2010, s. 13-44 [accessed 2017-12-28]. ISBN 978-1-84816-536-6. Available at: http://www.worldscibooks.com/materialsci/p703.html

[14] File:Scheme TEM en.svg. In: *Wikipedia* [online]. Wikimedia Commons, the free media repository. [accessed 2017-12-30]. Available at: https://commons.wikimedia.org/w/index.php?title=File:Scheme_TEM_en.svg&oldid=153399547

[15] File:Spherical aberration 3.svg. In: *Wikipedia* [online]. Wikimedia Commons, the free media repository., 2011 [accessed 2017-12-30]. Available at: https://commons.wikimedia.org/w/index.php?title=File:Spherical_aberration_3.svg&oldid=155599133

[16] GUANLEI, Xu, Wang XIAOTONG a Xu XIAOGANG. On analysis of bi-dimensional component decomposition via BEMD. *Pattern Recognition* [online]. 2012, **45**(4), 1617-1626. DOI: 10.1016/j.patcog.2011.11.004. ISSN 00313203. Available at: http://linkinghub.elsevier.com/retrieve/pii/S0031320311004535

[17] HAIDER, Max, Harald ROSE, Stephan UHLEMANN, Eugen SCHWAN, Bernd KABIUS and Knut URBAN. A spherical-aberration-corrected 200kV transmission electron microscope. *Ultramicroscopy* [online]. 1998, **75**(1), 53-60. DOI: 10.1016/S0304-3991(98)00048-5. ISSN 03043991. Available at: http://linkinghub.elsevier.com/retrieve/pii/S0304399198000485

[18] HALL, Peter, David MARSHALL and Ralph MARTIN. Adding and subtracting eigenspaces with eigenvalue decomposition and singular value decomposition. *Image and Vision Computing* [online]. 2002, **20**(13-14), 1009-1016. DOI: 10.1016/S0262-8856(02)00114-2. ISSN 02628856. Available at: http://linkinghub.elsevier.com/retrieve/pii/S0262885602001142

[19] HALLIDAY, David, Jearl WALKER and Robert RESNICK. *Fyzika: vysokoškolská učebnice obecné fyziky Elektromagnetické vlny-Optika-Relativita*. Brno: VUTIUM, 2000, p. 889-1032. Překlady vysokoškolských učebnic. ISBN 80-214-1868-0.

[20] HUANG, N. E., Z. SHEN, S. R. LONG, et al. The empirical mode decomposition and the Hilbert spectrum for nonlinear and non-stationary time series analysis. *Proceedings of the Royal Society A: Mathematical, Physical and Engineering Sciences*[online]. 1998, **454**(1971), 903-995. DOI: 10.1098/rspa.1998.0193. ISSN 1364-5021. Available at: http://rspa.royalsocietypublishing.org/cgi/doi/10.1098/rspa.1998.0193

[21] HUMEAU-HEURTIER, Anne, Guillaume MAHE and Pierre ABRAHAM. Multi-Dimensional Complete Ensemble Empirical Mode Decomposition With Adaptive Noise Applied to Laser Speckle Contrast Images. *IEEE Transactions on Medical Imaging*[online]. 2015, **34**(10), 2103-2117. DOI: 10.1109/TMI.2015.2419711. ISSN 0278-0062. Available at: http://ieeexplore.ieee.org/document/7079481/

[22] HYVÄRINEN, A. and E. OJA. Independent component analysis: algorithms and applications. *Neural Networks* [online]. 2000, **13**(4-5), 411-430. DOI: 10.1016/S0893-6080(00)00026-5. ISSN 08936080. Available at: http://linkinghub.elsevier.com/retrieve/pii/S0893608000000265

[23] HYVARINEN, Aapo., Juha. KARHUNEN and Erkki. OJA. *Independent component analysis*. New York: J. Wiley, c2001. 481 p. ISBN 04-714-0540-X.

[24] KARLÍK, Miroslav. *Úvod do transmisní elektronové mikroskopie*. Praha: České vysoké učení technické v Praze, 2011. 322 p. ISBN 978-80-01-04729-3.

[25] KUNDUR, D. and D. HATZINAKOS. Blind image deconvolution. *IEEE Signal Processing Magazine* [online]. 1996, **13**(3), 43-64. DOI: 10.1109/79.489268. ISSN 10535888. Available at: http://ieeexplore.ieee.org/document/489268/

[26] KUSHWAHA, Himmat S., Sanju TANWAR, K.S. RATHORE and Sumit SRIVASTAVA. De-noising Filters for TEM (Transmission Electron Microscopy) Image of Nanomaterials. *2012 Second International Conference on Advanced Computing & Communication Technologies* [online]. IEEE, 2012, 2012, , 276-281. DOI: 10.1109/ACCT.2012.41. ISBN 978-1-4673-0471-9. Available at: http://ieeexplore.ieee.org/document/6168375/

[27] MANJÓN, José V., Pierrick COUPÉ and Antonio BUADES. MRI noise estimation and denoising using non-local PCA. *Medical Image Analysis* [online]. 2015, **22**(1), 35-47. DOI: 10.1016/j.media.2015.01.004. ISSN 13618415. Available at: http://linkinghub.elsevier.com/retrieve/pii/S1361841515000171

[28] MITTAL, A., A. K. MOORTHY and A. C. BOVIK. No-Reference Image Quality Assessment in the Spatial Domain. *IEEE Transactions on Image Processing* [online]. 2012, **21**(12), 4695-4708. DOI: 10.1109/TIP.2012.2214050. ISSN 1057-7149. Available at: http://ieeexplore.ieee.org/document/6272356/

[29] Principle of an Electromagnetic Lens. In: *ETH zürich* [online]. [accessed 2017-12-30]. Available at: http://www.microscopy.ethz.ch/lens.htm

[30] RAJWADE, A., A. RANGARAJAN and A. BANERJEE. Image Denoising Using the Higher Order Singular Value Decomposition. *IEEE Transactions on Pattern Analysis and Machine Intelligence* [online]. 2013, **35**(4), 849-862. DOI: 10.1109/TPAMI.2012.140. ISSN 0162-8828. Available at: http://ieeexplore.ieee.org/document/6226423/

[31] Selected area diffraction pattern. In: *Warwick* [online]. [accessed 2017-12-30]. Available at: https://warwick.ac.uk/fac/sci/physics/research/condensedmatt/microscopy/research/researchthemes/d-ed/d-lacbed/d-lacbed_symmetry/

[32] STONE, James V. *Independent component analysis: a tutorial introduction*. Cambridge, Mass.: MIT Press, c2004. 193 p. ISBN 02-626-9315-1.

[33] Surface Fitting using gridfit. *MathWorks* [online]. Natick, Massachusetts: The MathWorks, c1994-2018 [accessed 2018-03-26]. Available at: https://www.mathworks.com/matlabcentral/fileexchange/8998-surface-fitting-using-gridfit

[34] TANCHENKO, Alexander. Visual-PSNR measure of image quality. *Journal of Visual Communication and Image Representation* [online]. 2014, **25**(5), 874-878. DOI: 10.1016/j.jvcir.2014.01.008. ISSN 10473203. Available at: http://linkinghub.elsevier.com/retrieve/pii/S1047320314000091

[35] TIMISCHL, F. The contrast-to-noise ratio for image quality evaluation in scanning electron microscopy. *Scanning* [online]. 2015, **37**(1), 54-62. DOI: 10.1002/sca.21179. ISSN 01610457. Available at: http://doi.wiley.com/10.1002/sca.21179

[36] TORRES, Maria E., Marcelo A. COLOMINAS, Gaston SCHLOTTHAUER a Patrick FLANDRIN. A complete ensemble empirical mode decomposition with adaptive noise. *2011 IEEE International Conference on Acoustics, Speech and Signal Processing (ICASSP)* [online]. IEEE, 2011, 2011, , 4144-4147. DOI: 10.1109/ICASSP.2011.5947265. ISBN 978-1-4577-0538-0. Available at: http://ieeexplore.ieee.org/document/5947265/

[37] WALEK, Petr, Martin LAMOŠ a Jiří JAN. *Analýza biomedicínských obrazů: Počítačová cvičení* [online]. 2. Brno, 2015. ISBN 978-80-214-4792-9.

[38] WANG, Z., A.C. BOVIK, H.R. SHEIKH and E.P. SIMONCELLI. Image Quality Assessment: From Error Visibility to Structural Similarity. *IEEE Transactions on Image Processing* [online]. 2004, **13**(4), 600-612. DOI: 10.1109/TIP.2003.819861. ISSN 1057-7149. Available at: http://ieeexplore.ieee.org/document/1284395/

[39] WILLIAMS, David B and C. Barry CARTER. *Transmission Electron Microscopy: A Textbook for Materials Science. Basic I*. New York: Plenum Press, 1996, 173 p. ISBN 0-306-45324-X.

[40] WILLIAMS, David B and C. Barry CARTER. *Transmission Electron Microscopy: A Textbook for Materials Science. Diffraction II*. New York: Plenum Press, 1996, p.177-345. ISBN 0-306-45324-X.

[41] WILLIAMS, David B and C. Barry CARTER. *Transmission Electron Microscopy: A Textbook for Materials Science. Imaging III*. New York: Plenum Press, 1996, p.349-549. ISBN 0-306-45324-X.

[42] WINKLER, Joab R. Polynomial computations for blind image deconvolution. *Linear Algebra and its Applications* [online]. 2016, **502**, 77-103. DOI: 10.1016/j.laa.2015.10.010. ISSN 00243795. Available at: http://linkinghub.elsevier.com/retrieve/pii/S0024379515006059

[43] WU, ZHAOHUA and NORDEN E. HUANG. ENSEMBLE EMPIRICAL MODE DECOMPOSITION: A NOISE-ASSISTED DATA ANALYSIS METHOD. *Advances in Adaptive Data Analysis* [online]. 2009, **01**(01), 1-41. DOI: 10.1142/S1793536909000047. ISSN 1793-5369. Available at: http://www.worldscientific.com/doi/abs/10.1142/S1793536909000047

[44] ZHANG, Lei, Weisheng DONG, David ZHANG and Guangming SHI. Two-stage image denoising by principal component analysis with local pixel grouping. *Pattern Recognition* [online]. 2010, **43**(4), 1531-1549. DOI: 10.1016/j.patcog.2009.09.023. ISSN 00313203. Available at: http://linkinghub.elsevier.com/retrieve/pii/S0031320309003677

[45] ZWORYKIN, V.K. *Electron optics and the electron microscope*. New York: John Wiley, 1945, 766 p.

List of abbreviations

ADF	annular dark field
AGGD	asymmetric generalized Gaussian distribution
ARMA	autoregressive moving average
BEMD	bi-dimensional empirical mode decomposition
BF	bright field
BLIINDS-II	blind image notator using DCT statistics
BRISQUE	blind/referenceless image spatial quality evaluator
CBED	convergent beam electron diffraction
CCD	charge coupled-device
CDF	centered dark field
CEEMDAN	complete ensemble empirical mode decomposition with adaptive noise
CNR	contrast-to-noise ratio
CRT	cathode ray tube
CTF	contrast transfer function
DF	dark field
DIIVINE	distortion identifiaction-based image integrity and verity evaluation
DP	diffraction pattern
EDS	energy dispersive X-ray spectroscopy
EELS	electron energy loss spectrometry
EEMD	ensemble empirical mode decomposition
EMD	empirical mode decomposition
EVD	eigenvalue decomposition
FastICA	fast Independent component analysis

fMRI	functional magnetic resonance imaging
GiT-BEMD	Green's function in tension-based bi-dimensional empirical mode decomposition
HAADF	high-angle annular dark field
HVS	human visual system
IC	independent component
ICA	independent component analysis
IMF	intrinsic mode function
IQA	image quality assessment
JAD	joint approximate diagonalization
JADE	joint approximate diagonalization of eigen-matrices
HRTEM	high resolution transmission electron microscopy
HR STEM	high resolution scanning transmission electron microscopy
LACBED	large angle convergent beam electron diffraction
MDEEMD	multi-dimensional ensemble empirical mode decomposition
MRI	magnetic resonance imaging
MSCN	mean subtracted contrast normalized coefficient
MSE	mean squared error
NADA	noise-assisted data analysis
NSS	natural scene statistics
OCT	optical coherence tomography
PC	principal component
PCA	principal component analysis
PCHIP	piecewise cubic Hermite interpolating polynomial
PED	precession electron diffraction
PSF	point spread function
PSNR	peak signal-to-noise ratio

TEM	transmission electron microscope
	transmission electron microscopy
SAD	selected area diffraction
sICA	spatial Independent component analysis
SNR	signal-to-noise ratio
SOBI	second order blind identification
SSIM	structural similarity index
STEM	scanning transmission electron microscope
	scanning transmission electron microscopy
SVD	singular value decomposition
SVR	support vector machine regressor
WBDF	weak-beam dark field
WPOA	weak-phase-object approximation
YAG	yttrium-aluminum garnet

List of symbols

a_{ii}	distance parameter
A	atomic weight
A	mixing matrix
A	noisy image
$A(\boldsymbol{u})$	aperture function
B	brightness
$\boldsymbol{B}$	magnetic field
$\boldsymbol{B}$	separation matrix
$B(\boldsymbol{u})$	aberration function
$c(\boldsymbol{x}, \boldsymbol{y})$	contrast comparison function
C	contrast
C	constant
C_C	chromatic aberration coefficient
C_S	spherical aberration coefficient
$\mathcal{C}_{\bar{x}}$	sampled contracted quadricovariance matrix
d	number of bits
d_z	diameter of the electron source
$d\sigma/d\Omega$	differential cross section of one atom
D	diagonal matrix for JAD
D_{im}	depth of focus
D_{ob}	depth of field
e	electric charge
e_{max}	upper envelope
e_{min}	lower envelope
eps	stopping criterion

E	expectation operator
$E_j(\cdot)$	operator for CEEMDAN method
$E(\boldsymbol{u})$	envelope function
$E\{\boldsymbol{x}\boldsymbol{x}^T\}$	covariance matrix
f	asymmetric generalized Gaussian distribution
f	focal length
$f(\boldsymbol{r})$	specimen function
F	original image
$F(\boldsymbol{u})$	Fourier transform of $f(\boldsymbol{r})$
$\boldsymbol{F}$	Lorentz force
g	tanh function, sigmoidal function
g	function used in ICA by negentropy
$g(\boldsymbol{r})$	image intensity
G	blurred image
$G(\boldsymbol{u})$	Fourier transform of $g(\boldsymbol{r})$
h	Planck constant
$h(\boldsymbol{r})$	point spread function
$h(i, j)$	EMD component within computing IMF
H	entropy
H	image dimension
H	point spread function
$H(\boldsymbol{u})$	Fourier transform of $h(\boldsymbol{r})$, contrast transfer function
I	current
$I(i, j)$	image with spatial coordinates i, j
I	intensity
I	mutual information
J	negentropy
$kurt(y)$	kurtosis of variable y

K	Kelvin
K	constant
$l(\boldsymbol{x}, \boldsymbol{y})$	luminance comparison function
L	range of pixel values
m	mass
M	magnification
N	noise
N_0	Avogadro's number
p	density
p	momentum
p	probability density function (pdf)
p	time lag
$p(i, j)$	pixel with neighborhood Ω
Q	cross section
Q_T	probability of scattering
$\boldsymbol{Q}$	orthogonalization matrix
$\mathbf{r}$	lattice vector
r_i	i^{th} residue in CEEMDAN algorithm
$R(i, j)$	EMD residue
R_{xx}	covariance matrix
r_{Sch}	point resolution
r_{th}	theoretical resolution
s	source signal, independent component
$s(\boldsymbol{x}, \boldsymbol{y})$	structure comparison function
S	area
t	thickness
$T(\boldsymbol{u})$	objective-lens transfer function
$\mathbf{u}$	reciprocal lattice vector

$\boldsymbol{U}$	orthogonal matrix of eigenvectors
v	shape parameter
v	eigenvector
$\boldsymbol{v}$	velocity
$\boldsymbol{V}$	orthogonal matrix of eigenvectors
V_w	whitening matrix
V_t	potential of the specimen of the thickness t
w	2D circularly-symmetric Gaussian function
w^i	i^{th} realization of white noise
$\boldsymbol{w}$	eigenvector
$\boldsymbol{W}$	demixing matrix
$\boldsymbol{W}$	weight matrix
$\boldsymbol{W}_{pca}$	matrix of eigenvectors
$\boldsymbol{x}$	signal mixture/observed vector
$\boldsymbol{x}$	reference image
X	input of the neural network
$\boldsymbol{y}$	distorted image
Y	output of the neural network
$\boldsymbol{z}$	whitened data
Z	atomic number
α	convergence semiangle
α	SSIM importance parameter
α_0	beam angle
α_i	value in ICA by maximum likelihood
β	semiangle of collection
β	SSIM importance parameter
β	variable in BRISQUE
β_i	value in ICA by maximum likelihood

γ	estimation of the kurtosis
γ	SSIM importance parameter
Γ	Gamma function
ΔE	electron energy variation
Δf	focal length variation
Δf_{Sch}	Scherzer defocus
Δf_{α}	distance of focal points
ΔI	current fluctuation
ΔV	initial velocity fluctuation
δ	theoretical resolution of microscope
ε_0	Gaussian noise standard deviation
θ	electron scattering angle
Λ	diagonal matrix of eigenvalues
λ	eigenvalue
λ	mean free path
λ	wavelength
μ	expectation value
μ	mean
ρ	density
Σ	pseudodiagonal matrix with singular values
σ	interaction constant
σ	variance
σ	standard deviation
σ	singular value
σ_T	total scattering cross section
σ^2	shape parameter
τ	threshold

$\chi(\boldsymbol{u})$	phase-distortion function
Ω	solid angle
Ω	pixel neighborhood
$\otimes$	convolution
$\mathbf{1}$	vector of ones

Appendix

Content of Included CD

There are the files on included CD:

- electronic version of this thesis
- Matlab scripts with implemented functions
- folder containing image dataset
- text document with instructions for functions